

CALIFORNIA STATE UNIVERSITY, NORTHRIDGE

SETTLING OF METAL DROPLETS THROUGH A MAGMA OCEAN AND METAL
PLUME CONDUITS DURING CORE FORMATION

A thesis submitted in partial fulfillment of the requirements
for the degree of Master of Science
in Geophysics

By

Danielle Brand

May 2014

The thesis of Danielle Brand is approved by:

Dr. Gerald Simila, Ph.D

Date

Ali Tabidian, Ph.D.

Date

Dayanthie S. Weeraratne, Ph.D., Chair

Date

California State University, Northridge

TABLE OF CONTENTS

SIGNATURE PAGE.....	ii
LIST OF TABLES.....	v
LIST OF FIGURES.....	vi
ABSTRACT.....	vii
Chapter 1: INTRODUCTION.....	1
Chapter 2: LABORATORY EXPERIMENTAL METHODS.....	8
2.1 Experimental Parameters.....	8
2.2 Experimental Design.....	8
2.3 Non-dimensional Numbers.....	12
2.4 Image Analysis.....	16
2.5 Locating the Lower Boundary and Upper Boundary.....	20
Chapter 3: RESULTS.....	22
3.1 Volumetric Ratio.....	22
3.1.1 Qualitative Features of the Three Stages of Separation.....	22
3.1.2 Time Evolution of the Mixture Layer.....	24
3.1.3 Fluid Entrainment.....	26
3.2 Density Difference.....	27
3.2.1 Droplet Velocities and Trajectories.....	27
3.2.2 The Lower Boundary Ascent Velocity.....	29
3.3 Metal Droplet Size.....	31
3.3.1 Edge Effects and Clustering.....	31
3.4 Viscosity of Ambient Fluid.....	33

3.4.1 Shear Force Dependence on Droplet Size.....	34
3.5 Fluid Entrainment Volume of Deformable Droplets Versus Rigid Spheres... <td>37</td>	37
Chapter 4: DISCUSSION AND GEOPHYSICAL IMPLICATIONS.....	39
4.1 Time of Metal Pond and Core Formation.....	39
4.2 Entrainment and Light Elements in the Core.....	46
4.3 The Siderophile Abundance Problem.....	49
4.4 Metal Sediment at the Core-Mantle Boundary.....	50
Chapter 6: SUMMARY.....	52
Chapter 7: FUTURE WORK.....	53
REFERENCES.....	55

LIST OF TABLES

1. Summary of Experimental Parameters.....	8
2. Fluid Properties.....	16
3. Summary of Values Used to Plot Figure 3.2 Theory.....	40

LIST OF FIGURES

Figure 1.1. Schematic diagram of emulsion settling locations.....	2
Figure 2.1. Schematic diagram of experimental apparatus.....	10
Figure 2.2. Visual of image analysis procedure.....	18
Figure 2.3. Time-lapse photographs of volumetric ratio experiments.....	19
Figure 2.4. Identifying the upper and lower boundaries.....	21
Figure 3.1. Migration of the upper and lower boundaries.....	24
Figure 3.2. Time of regime 1 and regime 2.....	26
Figure 3.3. Maximum height of the lower boundary.....	27
Figure 3.4. Droplet velocities and trajectories.....	29
Figure 3.5. Ascent velocity of the lower boundary.....	30
Figure 3.6. Particles size variance.....	33
Figure 3.7. Heights of the lower boundary for variable viscosities.....	34
Figure 3.8. Droplet size and shape changes for variable viscosities.....	36
Figure 3.9. Gallium debris layer.....	37
Figure 3.10. Rigid metal spheres versus liquid metal droplets.....	39

ABSTRACT

SETTLING OF METAL DROPLETS THROUGH A MAGMA OCEAN AND METAL PLUME CONDUITS DURING CORE FORMATION

By

Danielle Brand

Master of Science in Geophysics

The gravitational settling dynamics of molten iron droplets through silicate material is an important process during the early impact history of the Earth where settling may have occurred within magma oceans or within metal plume conduits descending rapidly to form the metallic cores in terrestrial bodies. Implications for equilibration of liquid metal in the silicate mantle are key in aiding our understanding of the thermo-chemical evolution of Earth. To simultaneously meet geochemical constraints for rapid core formation as well as siderophile trace element distribution throughout the upper mantle, an emulsion of iron droplets or an emulsion metal plume may be important. Previous experiments have shown that descending metal silicate plumes entrain magma ocean material in trailing conduits that travel to the core-mantle boundary. It has also been shown that the style of metal emulsions will descend through these conduits in two stages, as a coalesced group within the plume head and later settling through the conduit column. However, the nature of iron settling through a magma ocean and within conduits is only understood in a rudimentary way. Here, I consider physical fluid models which study the settling of liquid iron droplets through silicate melts using liquid gallium

emulsions and glucose solutions. I test the effect of several physical properties including the metal volumetric ratio, density difference, fluid viscosity, metal droplet diameter, and liquid versus solid metal spheres. Three stages are observed during gravitational settling. Regime 1 reveals rapid sinking of liquid metal droplets and entrainment of low-density (light element) fluids into a metal pond and into the core itself, regime 2 is characterized by upward migration of entrained fluid and regime 3 couples slow compaction of metal droplets at the base with final segregation of residual glucose solution. Results show that high volumetric ratios and low viscosity ratios of metal to magmas will have faster sinking velocities and metal pond or core formation times. I find that increased metal volumetric ratio and liquid (versus solid) metal spheres demonstrates more entrainment of magma into a metal pond or into the core. Higher levels of entrainment predicts the presence of light elements in the core during its formation and suggests “bottom-up” migration of light elements and metal-silicate segregation at high pressures during post core forming events. Upward migration of light elements will leave behind higher bulk density metals that initiate overturn in the outer core and can assist in powering the geodynamo. Finally, the settling process of emulsion metal droplets through magma oceans, plume conduits, and entrainment into the core provide a large surface areas and longer residence time for metal-silicate equilibration to address the excess siderophile observation while still descending rapidly enough to form the Earth's core in 30 My. I observe a metal sediment layer that forms above the metallic core after settling. If this sediment layer is stable, it may be entrained in upwelling mantle plumes over the Earth's history and contribute towards mixing of siderophile elements with mantle minerals.

Chapter 1. Introduction

Planetary formation and interior planetary differentiation remain mysterious processes despite their doubtless occurrence. Physical models of planetary accretion have shown that differentiation of terrestrial bodies is governed by rapid core formation (Wood et al. 2006). In the simplest model, Earth may have originated with chondritic composition and later segregated into two predominant materials – an iron core and a bulk silicate mantle. Geochemical chronometry constrains Earth’s core formation events to within 30-40 Ma (Kleine et al., 2002; Yin et al., 2002). Specifically, the currently observed abundance of short-lived isotopes such as ^{182}W relative to their non-radiogenic forms suggest an early, single stage, core formation age (Wood, 2006; Jacobson, 2005). During planetary differentiation, it is likely that metal descent occurred through multiple avenues such as sinking metal droplets from impact ejecta or whole scale merging of preformed cores. Here, I study the former case and consider three predominant scenarios, 1) iron metal emulsions settling through a magma ocean following meteorite impacts, 2) iron metal emulsions settling through metal plume conduits as Rayleigh-Taylor instabilities that descend to the core, and 3) the behavior of emulsion metal drops when they arrive at the core (see Figure 1.1).

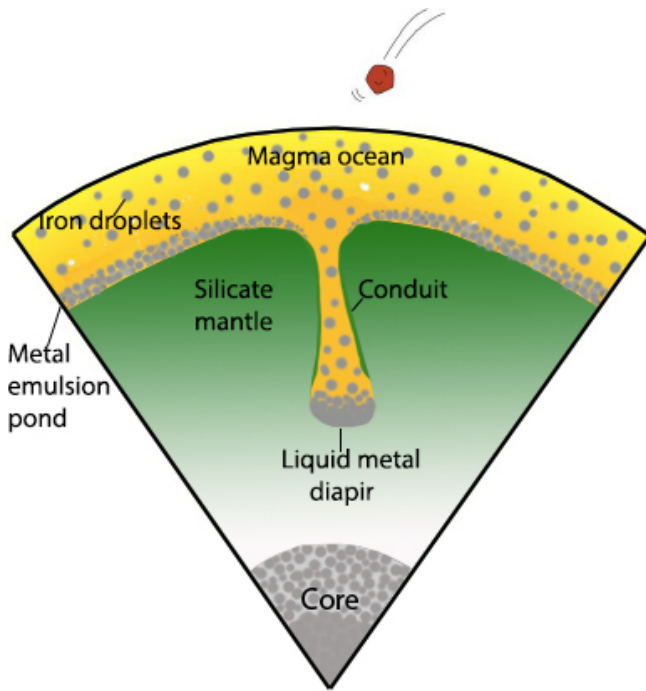


Figure 1.1. Schematic diagram of locations where liquid metal emulsions may be found during planetary differentiation. This study considers settling of iron in a magma ocean to form a metal emulsion pond, settling of iron emulsions through a trailing conduit for a descending metal plume, and the behavior of emulsions as they arrive at the core.

A period of intense meteorite bombardment and the decay of radionuclides likely provided enough energy for localized or widespread melting, forming magma reservoirs (> 400 km deep) or perhaps oceans of magma (Tonks and Melosh, 1993; Wood et al., 2006; Pahlevan and Stevenson, 2007; Solomatov, 2007; Rubie et al., 2003, 2007). Impacts dispersed metal and silicate particles that settled through the magma ocean and subsequently through the solid silicate mantle. The style of metal descent through the solid mantle is largely unknown and is often described analytically by equations (e.g. Stevenson, 1990) or oversimplified animations. The physics and assumptions in these calculations have never been verified in a physical setting, however. The settling of liquid iron droplets from meteorite ejecta may be of particular importance within magma oceans (Wood et al., 2006; e.g. Rubie et al., 2007) and during descent to the core (King and

Olson, 2011). Larger metal bodies from meteors having preformed cores underwent both buoyancy and shear instabilities in magma oceans with sufficiently high viscosities. It is argued that large bodies experienced emulsification at a downward vertical distance approximately equal to a few times its original diameter (Rubie et al., 2003).

Although many mechanisms have been proposed for metal descent and core formation, I summarize four major theories here. In the first case, small droplets percolate through a solid silicate mantle (Stevenson, 1990; Rushmer et al., 2000). However, percolation of small metal drops requires small dihedral angles between the molten iron and silicate minerals to produce permeability (Rubie et al., 2007), some degree of porosity or a considerable melt fraction coupled with significant shear stresses in the mantle (Honda et al., 1993). Petrologic studies have shown however, that the composition of mantle and core minerals at upper mantle pressures favor large dihedral angles (Kohlstedt and Zimmerman, 1996; Shannon and Agee, 1996; Minarik et al., 1996; Yoshino et al., 2003). These scenarios are likely to only occur at the base of the mantle. The second case may occur as descent through cracks in the mantle. Although this may be possible in the upper mantle, cracks are not likely to be present at deep mantle pressures where ductile deformation dominates. The final two cases suggest descent through large metal diapirs, either consisting of smooth metal diapirs (Stevenson, 1990) or metal emulsion diapirs (Fleck, 2011). In the final two cases, after gravitational settling, metal pooled at the base of the magma ocean above a silicate mantle. When sufficient metal volumes accumulated, the metal pond went unstable and began descent to the core (Stevenson, 1990). Trailing conduits were observed to form behind metal diapirs which are found to sink faster than the surrounding viscous mantle can collapse around it (Olson

and Weeraratne, 2008). In this study, low-density magma ocean fluid infills and is entrained to the base of the mantle (Nguyen et al., 2010). The significance of conduits is that they may provide a low-resistance path for core-forming metal transport in a high-viscosity mantle.

While conduit theory has been studied in previous models (Olson and Weeraratne, 2008; Nguyen et al., 2010; Rains et al., 2014) as large-scale flow in a planetary mantle system, the fluid mechanics of metal emulsion-silicate phase separation within a conduit is not well understood. Fleck (2011) investigated the instability of an emulsion metal pond. In these experiments, two stages of metal descent were observed, 1) immediate formation and descent of a metal emulsion diapir as a Rayleigh-Taylor instability, 2) a second stage of descent in the form of iron metal rain of droplets far from the initial instability site. In stage 2, droplets that are on the fluid-fluid interface far from the site of downwelling, later descend and rain through the conduit and through the ambient fluid surrounding the conduit as well. Return flow of the buoyant entrained material to the surface is later observed once the diapir reaches the base where metal-silicate segregation occurs analogous to a model of the first upwelling mantle plumes in a planetary interior. However, the details of metal emulsion settling to form the metal pond (later settling through the conduit) and metal-silicate segregation throughout these processes are not well understood. Phase separation of binary fluids with similar densities and a relatively small interfacial surface tension ($<41 \text{ mJ/m}^2$) has previously been studied by Sato & Sumita (2007) using oil and water. This study finds that coalescence and phase separation is dependent on the volumetric and viscosity ratios of the descending and continuous phases. However, this study does not consider the behavior of high-density liquid metal

separating through low-density solutions with a large interfacial surface tension, as is characteristic of early magma oceans. Surface tension becomes important because at higher magnitudes, coalescence of droplets will be delayed or inhibited.

The settling of metal droplets through silicate melts is also important because it can determine the chemical and thermal re-equilibration history of planetary differentiation (Rubie et al., 2003; Karato and Murthy, 1997). Today, it is known that there is an excess abundance of siderophile elements in the upper mantle such as W, Ni, and Co (Ringwood, 1966). Partial chemical equilibration between metal and silicates is shown to occur (Chabot et al., 2005) at temperatures and pressures of approximately 2500 K and 30-40 GPa respectively (Righter & Drake, 2000). One possibility is that this indicates a magma ocean depth of ~400 km is where re-equilibration takes place. Several theories have been proposed as a solution to the “excess siderophile element problem” including, 1) inefficient core formation, 2) heterogeneous accretion, and 3) high-pressure core formation (Wood et al., 2006). Here, I consider small metal droplet emulsions settling through silicate melt after a period of meteorite bombardment (e.g. Stevenson, 1990). In a magma ocean, equilibration of small (~1 cm) metal droplets (Rubie et al., 2007) and silicate melt transpires on an accelerated scale relative to segregation of large metal bodies through a sub solidus liquid mantle (Höink et al., 2006). Small metal droplets fall at a slower velocity compared to larger metal bodies and provide more mass diffusion time for equilibration in a magma ocean (Rubie et al., 2003). However, small droplets may fall in groups (Olson & Weeraratne, 2008; Fleck 2011) that are sufficiently fast to meet the requirements of short core formation times. Small droplets also contribute a larger surface area over which chemical reactions between metal and silicate phases can

occur. An increase in liquid metal-silicate melt surface interaction and longer settling times may explain the currently observed widespread abundance of excess siderophile elements in the upper mantle.

Metal emulsions settling through conduits have further application to present day core superheat (+ 1000 K). Shear heating due to fast settling velocities and viscous dissipation causes metal droplets to retain their heat at distances that may extend all the way to the core. Thermal equilibration time of metal emulsion droplets is shown to be small relative to their settling time (King and Olson, 2011) whereas large metal diapirs have larger diffusion distances. In this way, the descent of small metal emulsion drops may create more super heat that is transported to the core compared to descent of a large diapir.

Finally, I will show that metal emulsions may have implications for density deficiencies in the core. Light elements such as S, O, Si, C, P, and H likely comprise up to 10% of core material since it is known that Earth's core density is low by roughly 5-10% (Birch, 1952; Anderson and Isaak, 2002). Being able to constrain Earth's core chemical composition is important for understanding processes which occur at the core mantle boundary (CMB) (Buffet et al. 2000; Helffrich and Kaneshima, 2004). Experiments on metal droplets may explain mechanisms of light element transport to the core via entrainment.

The settling dynamics of deformable metal droplets has not been robustly studied in laboratory simulations. My experiments isolate the metal-silicate phase system using liquid gallium and glucose fluid solutions to study liquid iron metal settling through magmas in a magma ocean and a trailing conduit. These experiments are designed to

carefully test fluid and settling behavior over a range of physical parameters (Table 1) using immiscible fluids with high-density contrasts and large interfacial surface tension ($\sim 735 \text{ mJ/m}^2$) in order to scale experiments more closely to early Earth conditions. These experiments will explore liquid metal settling through magmas of different volume ratios, fluid densities, fluid viscosities, and particle sizes. Estimates for magma viscosities and densities in these scenarios span a wide range (e.g. Solomatov, 2000; Fu and Elkins-Tanton, 2014), therefore, I consider flow dynamics in both the low and high Reynolds number regime governed by Stokes and Darcy flow, respectively. My experiments show that larger volumes of metal emulsions entrain more low-density conduit material. This entrainment may provide an explanation for the transport and presence of light elements (REFS) in the core today. The volumetric ratio of metal-silicate material will also have a direct affect on core growth times. Tests using both liquid and solid metal spheres show that iron liquid drops will entrain more silicate magma material than solid spheres. For liquid metal experiments, the slow compaction of metal emulsion at the CMB suggests interstitial silicate fluid is in contact with metal for a prolonged period of time, allowing more silicate-metal equilibration before upward migration. Sufficient time for metal-silicate equilibration in the core may offer further explanation for light elements in the core. Lastly, I show that small droplets fall at reduced velocities and provide larger surface interaction between the metal and silicate phases, thus providing reason for the excess abundance of siderophile elements in the upper mantle.

Chapter 2. Laboratory Experimental Methods

2.1 Experimental Parameters

Four series of experiments are preformed and fluid behavior is closely measured in each case. Specifically, I investigate gravitational phase separation of liquid gallium emulsions from glucose solutions as a function of volumetric metal fraction, fluid density, fluid viscosity, and metal droplet radius. The latter two experiments are done with rigid metal spheres due to difficulty isolating viscosity from droplet radius using experimental methodology in my study (as discussed below). The range in variation for each set of parameters is summarized in Table 1.

Parameter	Symbol	Unit	Range
Volumetric ratio (gallium/glucose)	$\psi = \psi_m / \psi_f$	-	10% - 35% metal
Density difference	$\Delta\rho = \rho_m - \rho_f$	g/cm ³	4.305 - 6.761
Viscosity of glucose (at 37° C)	μ	Pa s	0.03 - 80.0
Metal sphere diameter	d	cm	0.12 - 0.95

Table 1. Summary of experimental parameters and the range of variation used for experiments. The volumetric ratio is given by the volume of metal (ψ_m) and ambient fluid (ψ_f) respectively. Density difference is given by $\Delta\rho$ defined as the difference between liquid gallium metal density (ρ_m) and glucose solution density (ρ_f).

2.2 Experimental Design

I study the settling of liquid metal droplets through a tall rectangular tank filled with glucose solution. The plexiglass tank is 36.5 cm high, 4.5 cm x 4.5 cm in area and

has a wall thickness of 1.1 cm. This tank is narrow to accommodate small volumes of gallium which is costly. However droplet radii (see Table 1) in my experiments are significantly smaller than the box dimensions allowing us to minimize edge effects especially in the middle of the tank. The tank is filled with glucose solution and the appropriate amount of liquid metal gallium. To convert a smooth liquid volume of gallium into emulsion droplets, I pour the liquid gallium into a container of viscous glucose solution and agitate it which causes the liquid metal to break apart. A specially designed apparatus for agitating holds the fluid column between two clamps and is manually rotated about a pivotal axis forward and backward 180°. A regular rate of agitation is maintained using a metronome set to 60 BMP and agitation proceeds until a uniform metal emulsion forms. The fluid column is subsequently brought to an upright position, marking the start of the experiment. Note that initial experimental conditions have been tested to investigate the possibility of momentum imparted to fluid particles due to this rotation and agitation process but were found to be negligible. This is confirmed because particle velocities would be faster at the top and slow down in the middle of the box where they reach terminal velocity. However, measurements of particle velocities show that this is not the case, but rather the opposite. Using this method, a three-layered structure is created that evolves during settling into 1) a liquid gallium layer of emulsified metal that forms quickly at the base, 2) a mixture layer of liquid gallium droplets and glucose that forms in the middle, and 3) a layer of glucose solution that grows at the top (Figure 2.1). I define the interface between the liquid gallium layer and the mixture layer as the lower boundary (**LB**) and the interface between the mixture layer and the glucose layer as the upper boundary (**UB**). Metal droplets are allowed to settle

and compact for several days, although the majority of the material settles within 5 - 10 minutes. The experiments are backlit with an LED light panel and rapid time-lapse photographs are taken using a digital camera. Since corn syrup is transparent and gallium is opaque, the light panel enhances visualization of the two-phase system.

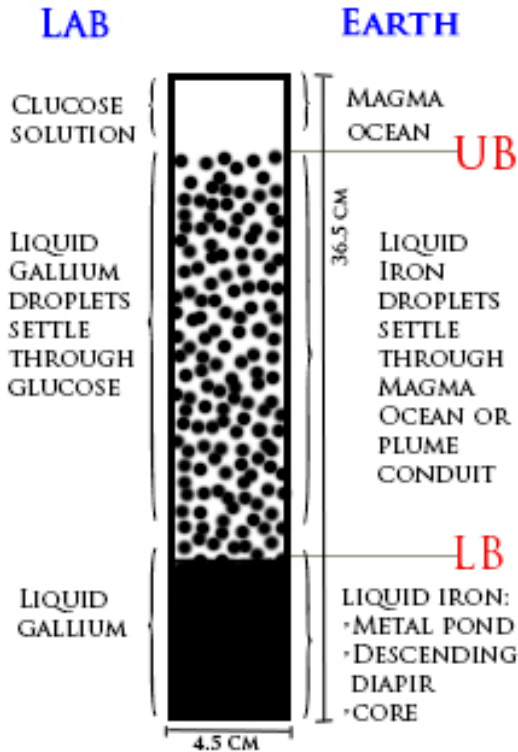


Figure 2.1. Schematic diagram of experimental apparatus. Three layers form that are separated by an upper boundary (**UB**) and a lower boundary (**LB**). A plexiglass box is used with dimensions 4.5 cm x 4.5 cm x 36.5 cm. The wall thickness is 1.1 cm.

To achieve a full range of fluid viscosities, I dilute standard grade corn syrup with varying amounts of water. The highest viscosity (80 Pa s) is obtained by heating corn syrup in order to allow for water evaporation. After mixing or evaporating, the fluid is poured into a graduated cylinder. Density is measured using a hydrometer and viscosity is measured using the falling ball method for Stokes fluids. The diameter of the graduated

cylinder is sufficiently large to eliminate wall effects. This method is repeated 4-8 times for each fluid and averaged for accuracy. Ambient fluid viscosity is then calculated using Stokes law for a rigid sphere

$$\mu = \frac{2a^2(\rho_b - \rho_f)g}{9V} \quad (1)$$

where a is the radius of the ball, ρ_b is the density of the ball, ρ_f is the density of the ambient fluid, g is gravitational acceleration, and V is the ball drop velocity.

The density of glucose solutions is varied with the addition of sodium bromide. This is achieved by dissolving sodium bromide in heated water to create saturated solutions of varying amounts, then mixing these solutions with pure glucose syrup. To vary the metal volume, liquid gallium (purity 99.99%) is used in six different quantities as given in Table 1. All experiments are conducted at 37°C in an insulated, temperature controlled environment in order to maintain gallium as a liquid phase. The density of liquid gallium is approximately 5.91 g/cm³ and has a viscosity of approximately 2.0 x 10⁻³ Pa s at its melting point of 29°C. The interfacial surface tension of liquid gallium is roughly 700 mJ/m². Gallium is convenient to use because it allows for experimentation with metal in a liquid state at near room temperature. For the viscosity variance and particle size variance experiments, stainless steel, rigid spheres (with density 7.991 g/cm³) are employed. Since variations in liquid gallium particle size are obtained by agitation with different viscosity glucose solutions, these two parameters cannot be divorced. Precision stainless steel balls ensure a uniform droplet size while keeping viscosity constant. Similarly, when varying fluid viscosity rigid metal spheres are used to

keep the droplet size constant. The added benefit is that I am also able to compare the settling of solid versus liquid metal spheres for experiments with similar droplet size and fluid viscosity.

2.3 Non-dimensional Numbers

Several non-dimensional numbers are used to characterize and scale experiments. I use the Bond number (Bo) to determine the importance of droplet shape in my experiments

$$Bo = \frac{\Delta\rho g a^2}{\sigma} \quad (2)$$

which compares buoyancy forces to interfacial surface tension. Since surface tension acts to restore droplets to a spherical shape, the Bo determines when buoyancy forces are large enough to dominate and cause shape changes that deviate from spherical. Here $\Delta\rho$ is the density difference between metal and ambient glucose fluid, g is gravitational acceleration, a is the droplet radius, and σ is surface tension. Experimental Bond numbers range from $2.4 \times 10^{-4} - 3.7 \times 10^{-4}$ and Bond numbers on Earth range from $2.8 \times 10^{-4} - 1.8 \times 10^{-3}$ (see Table 2). In laboratory experiments, surface tension dominates and droplets are approximately spherical when not in contact with one another. When sufficiently low viscosity fluids are used (between $0.01 \text{ Pa s} - 1.0 \text{ Pa s}$), coupled with high metal volume experiments, increased interaction between particles causes temporary deformation. Droplet deformation is important because it acts to prevent coalescence as droplets come

in contact with each other and controls the ambient fluid drainage velocity (Sato & Sumita, 2007).

The Reynolds number (Re) is used to compare inertial forces to viscous forces.

$$Re = \frac{\rho V L}{\mu} \quad (3)$$

Here, ρ is the droplet density, V is the droplet velocity, L is the droplet radius, and μ is the viscosity of ambient fluid. Stokes flow theory is relevant for Reynolds numbers < 1 where viscous forces are dominant and inertial forces are negligible. Stokes flow velocity in porous media is given as

$$V_{st} = \frac{a^2 \Delta \rho g \phi}{3\mu} \quad (4)$$

where a is the droplet radius, ϕ is porosity and the coefficient $C = 1/3$ is for a deformable liquid drops or a bubble. Solid spheres demonstrate more shear resistance, increased drag, and have a smaller coefficient of $C = 2/9$. This describes the velocity of a single drop falling through a container of fluid (rather than a volumetric flow rate as is the case with Darcy flow below). Hydraulic gradient is ignored since terminal velocity and constant pressure are assumed. Stokes flow is characterized by relatively large viscous forces where drag is important and inertia is negligible.

For Reynolds numbers > 1 where viscous forces are negligible and inertial forces are principal, Darcy flow velocity in porous media is applicable and is given by

$$V_d = \frac{K_\phi \Delta \rho g}{\mu} \frac{dh}{dx} \quad (5)$$

where K_ϕ is permeability and dh/dx is the hydraulic gradient. Darcy velocity considers volumetric flow rate per unit area and applied pressure. Viscous forces are characteristically small in Darcy flow and inertia dominates. This also requires laminar flow within pore spaces and drag forces are generally small or neglected.

Experimental Reynolds numbers range from $1.9 \times 10^{-4} - 1.2 \times 10^2$ indicating that my experiments span both the Stokes and Darcy flow regimes. Typical Reynolds numbers for the Earth are applicable to metal emulsions settling through a magma ocean and range from $1.6 \times 10^{-4} - 2.4 \times 10^{11}$ depending on the range of viscosities, densities, and droplet sizes estimated for a magma ocean (e.g. Solomatov, 2000; Rubie et al., 2003; Olson and Weeraratne, 2007; Fu and Elkins-Tanton, 2014). These Re values for the Earth also bridge both the Stokes flow and Darcy flow regimes. Thus I consider both cases in theoretical comparisons with laboratory observations.

Finally, I consider the viscosity ratio λ , volumetric ratio ψ , and buoyancy ratio β

$$\lambda = \frac{\mu_m}{\mu_f} \quad (6)$$

$$\psi = \frac{V_m}{V_f} \quad (7)$$

$$\beta = \frac{\rho_m}{\rho_f} \quad (8)$$

where μ_m , V_m , and ρ_m are the metal viscosity, volume and density respectively and μ_f , V_m , and ρ_m are the continuous phase fluid (glucose solution) viscosity, volume and density respectively. In the case of rigid spheres, the viscosity ratio is infinite and droplets do not deform. For finite viscosity ratios, the drainage between droplets is a function of λ , which further affects efficiency of droplet coalescence (Chesters, 1991; Wang et al., 1994; Yoon et al., 2005). For $\lambda \ll 1$, the boundary between the droplet and the continuous phase fluid becomes stress free (fully mobile) and plug flow produces rapid drainage. Conversely, for $\lambda \gg 1$ (as is the case for rigid spheres), the boundary condition becomes immobile and drainage is slow due to parabolic flow (Sato & Sumita, 2007). In my experiments, intermediate λ values ($\sim 10^{-1}$) suggest that contributions from both plug and parabolic flow occur. Previous studies using non-metallic fluids suggest that deformation of droplets (e.g. dimpling or flattening) may occur and drainage velocity is further slowed (Yiantsios & Davis 1990). However this is not observed directly in my experiments with liquid metal phases where surface tension is high. Laboratory and Earth ranges for fluid properties are summarized in Table 2.

Property		Unit	Lab	Earth
Glucose/ MO viscosity	μ_f	Pa s	0.01-80	10^{-2} - 100
Metal viscosity	μ_m	Pa s	2×10^{-3} (Ga)	1.0×10^{-3} - 3.0×10^{-3} (Fe)
Glucose/ MO density	ρ_f	g/cm ³	1.23 - 1.605	2.45 - 2.95
Metal density	ρ_m	g/cm ³	5.91 (Ga) - 7.991 (Steel)	7.0 - 9.0 (Fe)*
Density difference	$\Delta\rho$	g/cm ³	4.305 - 6.761	4.05 - 6.55
Bond number	Bo	-	2.4×10^{-4} - 3.7×10^{-4}	2.8×10^{-4} - 1.8×10^{-3}
Reynolds number	Re	-	1.9×10^{-4} - 1.2×10^2	1.6×10^{-4} - 2.4×10^{11}
Surface tension	σ	mJ m ⁻²	700 (Ga)	900 (Fe-Silicate)
Viscosity ratio	λ	-	2.5×10^{-5} - 2.0×10^{-1}	1.0×10^{-5} - 3.0×10^{-1}
Volumetric ratio	ψ	-	0.1 - 0.35	0.01-0.1
buoyancy ratio	β	-	3.68 - 6.50	2.37 - 3.67

Table 2. Summary of fluid properties. Magma ocean is abbreviated as MO. * The density of iron varies from mantle depths to core depths. A density of 7.0 g/cm³ is assumed in these experiments.

2.4 Image Analysis

Images are analyzed to quantify fluid phase separation using ImageJ software. I write a program that identifies and differentiates images of gallium and glucose solutions during settling. Parameters such as average droplet size, count, distance, velocity, position and fluid area can be measured as a function of time or height within the fluid column. This is key to identifying phase boundaries of the mixture layer and the extent of lateral phase separation

Photographs are cropped so that only material in the fluid column is used for image analysis. Each fluid column is separated into fifty slices (0.73 cm in height and 4.5 cm in width). A series of data is collected for each image or slice. The program commands are shown visually in Figure 2.2 and are summarized below.

1. A measurement scale is determined in the pixelated image using a ruler placed adjacent to the front pane of the experimental box that is visible in the photo image. The images used have the equivalent of 135 pixels to 1 cm. This scales the image dimensions to laboratory units and measurements are reported in centimeters.
2. Image J options, *8-bit conversion*, converts the image into 255 shades of gray, where 0 = pure black and 255 = pure white.
3. Image J option, *thresholding*, detects edges of dark (metal) material.
4. The image is converted into a binary black and white scheme using the edges from thresholding. (The example shown below inverts the black to show the continuous fluid area and white to show the gallium area.)
5. The black areas are selected.
6. Image analysis of “black” versus “white” areas is performed.

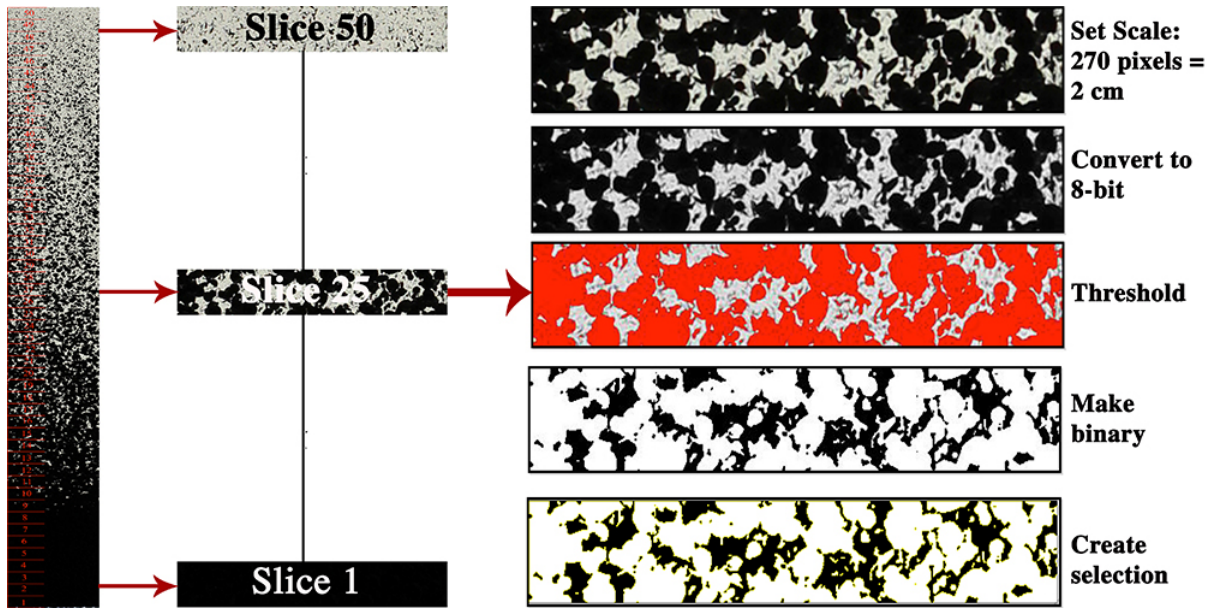


Figure 2.2. Visual of image analysis procedure. Left) The fluid column is broken up into 50 slices within which images analysis is performed. Middle) Three example slices are shown for slice 1, 25, and 50. Right) Each step of the image analysis is shown at the right for box slice 25 as described in the text.

I follow similar methods as described by previous laboratory experiments (Sato and Sumita, 2007) to perform image analysis. Their fluid experiments focus on the separation dynamics of oil-water mixtures by varying volumetric and viscosity ratios in order to study the fluid-fluid separation process. The separation of immiscible fluids is an important process during planetary differentiation. However, for applications to differentiation processes in the Earth during core formation, I consider liquid metal (gallium) and glucose fluid phases. In order to study settling processes of liquid metal droplets through a continuous phase glucose solution, I track the heights of the upper and lower boundaries (Figures 2.1 and 2.3) with time. The upper boundary descends with time due to the settling out of gallium droplets while the lower boundary rises due to the accumulation of gallium droplets at the base of the box. The middle region between the

upper and lower boundary is termed the *mixture layer*. The time evolution of boundary heights is monitored and acts as a guide for measuring separation rates and other fluid behavior.

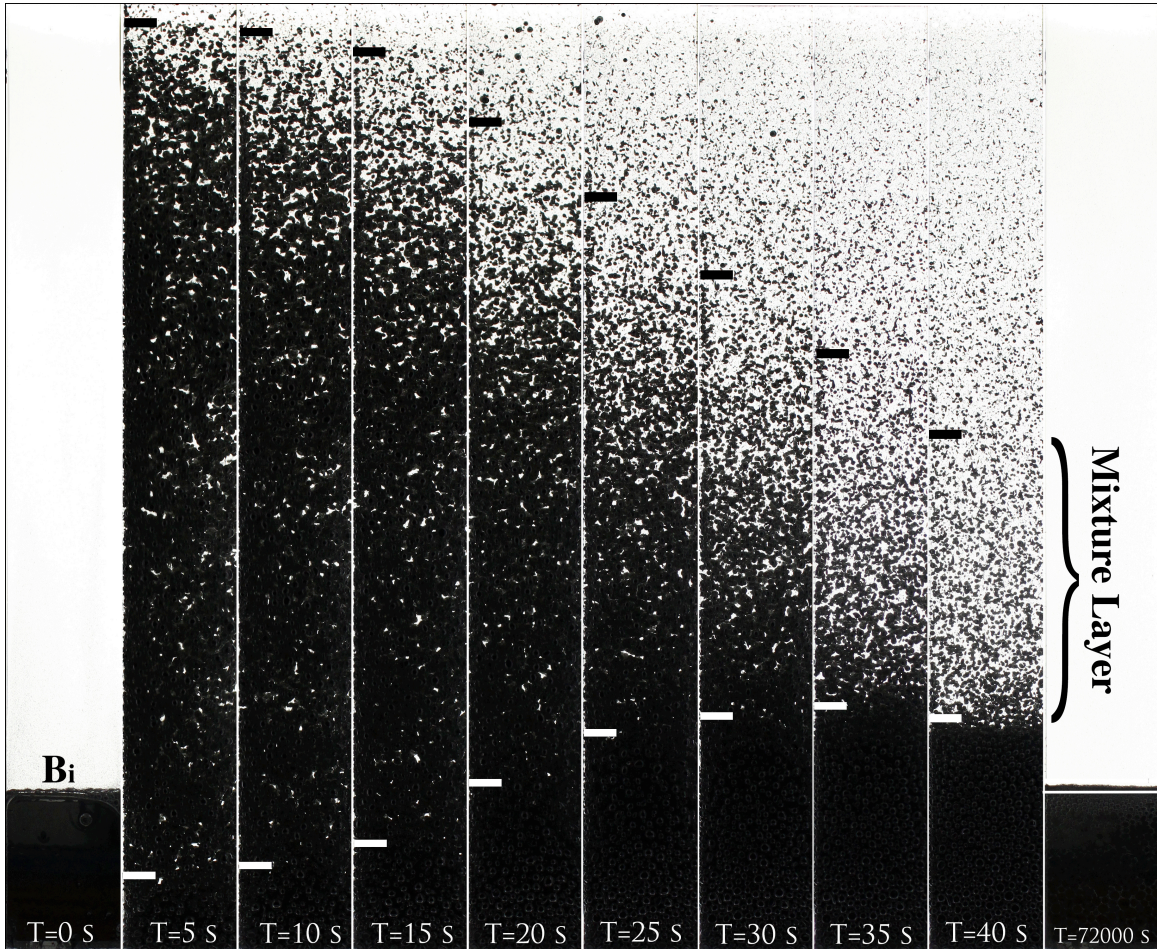


Figure 2.3. Time-lapse photographs of variable volumetric ratio experiments. The tank is 36.5 cm in height and 4.5 cm x 4.5 cm in area. The numbers indicate time elapsed since the experiment onset. The volumetric fraction of gallium is $\psi = 0.25$ with droplets of gallium having an average diameter of $d = 0.27$ cm. Glucose viscosity and density difference is of $\mu = 1.3$ Pa s and $\Delta\rho = 4.58$ g/cm³ respectively. When gallium droplets start to segregate (after T=0), the lower boundary (**LB**) ascends due to downward entrainment of glucose and accumulation of metal. The upper boundary descends due to settling of metal droplets. The upper boundary (**UB**) descends due to settling of metal droplets. White bars indicate position of the **LB** with time and black bars indicate position of the **UB**. The white line in the first and last frames indicates the position of the initial boundary (**Bi**). The final boundary is 0.188 cm higher than the initial boundary.

2.5 Locating the Lower Boundary and Upper Boundary

To locate the lower boundary, I take advantage of the distinct dark (gallium) versus light (glucose) areas in images. Light refracts through the translucent glucose solution only. I write an ImageJ routine (see section 2.4.1) that recognizes the two separate phases and determines the area of the continuous glucose solution in each box slice and outputs the values as a function of box height. The area of the continuous glucose phase is plotted as a function of height in Figure 2.4a. Two distinct trends are observed with distinctly different slopes. The continuous glucose phase is absent for heights up to 20 cm where the area is zero. This slope changes sharply at 20 cm and shows a positive slope with positive area values for the continuous phase. This is the point at which glucose area is measurable. This point is used to determine the position of the lower boundary and is interpreted as the interface below which liquid gallium fills the box (and no light penetrates). This analysis is done for every box slice and for many columns as a function of time. Note that I discuss below the presence of small amounts of glucose fluid that is sometimes present below the lower boundary interface, perhaps at grain boundaries between emulsion drops. However, light does not penetrate through the droplet packing structure in such small percentages at this depth.

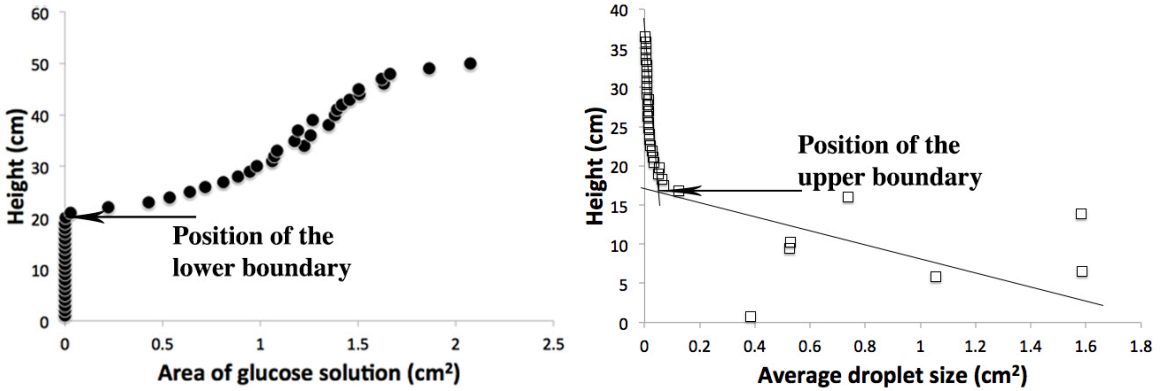


Figure 2.4. Image analysis data to identify the lower boundary (**LB**) and upper boundary (**UB**) of the fluid phases during settling. (a) The two-dimensional area of glucose solution is plotted as a function of height in the box and is used to identify the position of the **LB** for the same experiment as in Figure 2.3. The error in height is 0.73 cm (one standard error) which is approximately the symbol size. The error in glucose area ranges from 0.14 - 0.21 cm² as ψ varies from 0.1 – 0.35. For both (a) and (b), the volumetric ratio of gallium is $\psi = 0.25$, droplets of gallium have an average radius of $d \sim 0.27$ cm \pm 0.21 cm, (the standard error in hand-selecting and drawing circles around each particle will be determined), the glucose viscosity is $\mu = 1.3$ and the density difference is $\Delta\rho = 4.48$ g/cm³. a) A time shot at 20 s and the arrow indicates where the **LB** is defined. Below the **LB**, gallium fills the box and above the **LB**, the mixture layer begins. Here, this occurs at ~ 20 cm. (b) The average droplet size is plotted as a function of height to identify the position of the **UB**. The **UB** is defined at the intersection of the two data points. Plot (b) represent a time shot at 60 s and the arrow indicates where the **UB** is defined. Below the **UB** is the mixture layer and above the **UB** is the glucose layer. Here, the **UB** position occurs at ~ 17 cm. This process is repeated for each photo images as a function of time in order to plot the **UB** and **LB** behavior as shown in Figure 3.1.

Locating the upper boundary is more challenging than the lower boundary, partially because it is more diffuse and less clearly defined (Figure 2.3). This is the location wherein gallium droplets are no longer observed but where small flakes of gallium debris linger in the glucose layer. During the agitation process, both gallium droplets and gallium residue flakes (or debris) form due to viscous shear stresses with the continuous glucose phase. However, this metal debris is not a significant amount of metal volume. These gallium metal flakes have shapes that are non-spherical which makes them susceptible to increased drag. Therefore, this debris is observed to settle more

slowly, lingering in the uppermost glucose layer longest. In order to locate the upper boundary, a threshold is identified above which only gallium debris exists. This can be done by measuring particle size in each box slice as shown in Figure 2.4b. This threshold ranges from $0.05 - 0.15 \text{ cm}^2$ and is unique for each experiment depending on how much gallium debris develops. The average particle size of gallium (generated by ImageJ) is plotted as a function of box height and a sharp change in slope occurs (Figure 2.4b) at this threshold. The intersection between the two sloping lines is interpreted to be the ***UB***, giving the box height at which particles are sufficiently small and are no longer considered to be droplets but rather are defined as debris or residue. This box height matches well with visual inspection. I further confirm the distinction between gallium droplets and gallium debris by measuring their free-fall velocities. Debris falls at a much slower rate than droplets do but faster than glucose fluid.

Chapter 3. Results

3.1 Volumetric Ratio

3.1.1 Qualitative Features of the Three Stages of Separation

Emulsion behavior is largely determined by the volumetric fraction of the dispersed (liquid gallium) phase (Lowenberg, 1998). I conduct a series of experiments that vary volumetric ratios of the two fluids. The volume ratio of gallium to the continuous phase solution in mixtures is defined as ψ (7) and is varied from 10 % to 35%. The ***LB*** and ***UB*** heights are tracked with time (following methods described above in Chapter 2) and plotted in Figure 3.1 for the experiment where $\psi = 25\%$. The data reveal

three regimes of fluid behavior that are observed during the settling process. Regime 1 (R1) reveals rapid sinking of metal droplets and a simultaneous swift rise of the **LB**. Notice the maximum height of the **LB** (LB_{max}) exceeds the initial boundary (B_i). I suggest that this occurs because of entrainment of the glucose solution around metal droplets, increasing the total fluid volume below the **LB** upon initial descent. In regime 2 (R2), the **LB** reverses and decreases with time (at a slower rate than it formed in R1). I suggest this is due to migration of glucose solution upwards through the liquid metal matrix. Finally, in regime 3 (R3), a very slow decrease of the **LB** is observed until it approaches the initial boundary (B_i). In this phase, I suggest that compaction and coalescence of liquid metal droplets occurs, releasing the last amounts of glucose solution through upward migration and depresses the **LB**. This is the phase wherein final segregation of residual glucose solution occurs. Through all three stages, the **UB** decreases at a roughly steady rate within error. At long times, the upper boundary approaches B_i signifying that the mixture layer completely disappears and all gallium (including metal residue and debris) has settled to the base.

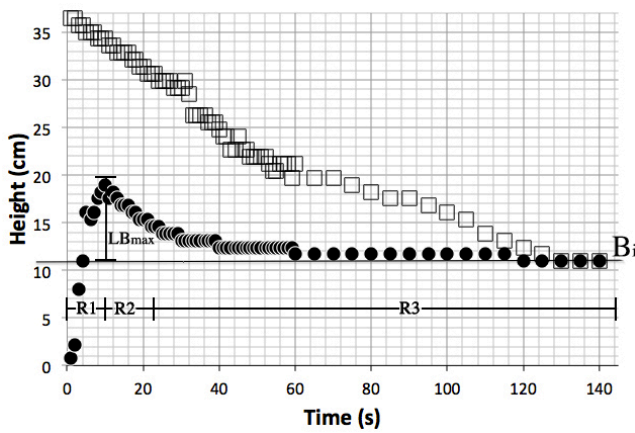


Figure 3.1. Migration of the **LB** (open circles) and descent of the **UB** (open squares) corresponding to the experiment with volumetric ratio of gallium $\psi = 0.25$ (also shown in

Figure 2.4). Glucose viscosity and density difference are held constant at $\mu = 1.3 \text{ Pa s}$ and $\Delta\rho = 4.58 \text{ g/cm}^3$ respectively. Gallium droplets have an average diameter of $d = 0.27 \text{ cm}$ and $Re = 0.81$. Plotting the positions of the **UB** and **LB** as a function of time shows that the **LB** rises rapidly within the first 10 s, exceeds the initial boundary (B_i), and reaches its peak. This initial phase of the separation process is defined as regime I (R1). The boundary then reverses and decreases at a slower rate from 10 s - 40 s, during regime 2 (R2). At times beyond 40 s, the boundary descends exponentially slower until it returns to the initial boundary. I define this final phase of the separation process as regime 3 (R3). The upper boundary decreases at a roughly steady rate. The error in height is 1.5 cm (two standard errors) and is approximately twice the height of a symbol. The error in time is 0.3 s based on the number of frames per second captured in photographs.

3.1.2 Time Evolution of the Mixture Layer

In Figure 3.2, the settling time of mettle droplets in regime 1 and upward migration time of glucose solution in regime 2 is shown with respect to increasing metal volume. Regime 1 and regime 2 are of particular interest when tracking the evolution of the mixture layer because more than 70 % of settling occurs before the onset of regime 3. Settling times for regime 1 are observed to decrease slightly with increasing volumetric ratio (Figure 3.2a). Stokes settling velocity adapted for porous media (4) is shown by the dashed line. Here, flow through porous media is approximated by considering gallium volume porosity (ϕ_m) which is a percentage of the total area of the box. This is determined through image analysis of the metal phase in the mixture layer for regime 1. Stokes velocity predicts the same slope of the data that I observe, but predicts slightly shorter settling times. Using particle-tracking methods, I show that increased fluid volumes may present more particle-particle interaction. This Brownian motion is not included in Stokes theory and will act to slow particles which would otherwise have a vertical descent trajectory. A Reynolds number of 0.81 is calculated only for the case of $\psi = 0.1$. However, due to the increasing **LB** velocity in regime 1, it is expected that the Reynolds number will increase with increasing volumetric ratio. More analysis will be

done to obtain Reynolds numbers for all experiments and determine if Reynolds number are greater than 1 (Darcy flow).

The time for regime 2, however, increases with increasing ψ (Figure 3.2b).

Regime 2 describes the time for upward migration of the continuous phase that has been entrained by liquid gallium droplets below the LB . As the fluid migrates upwards, the LB decreases from its maximum height as shown in Figure 3.1. I show the predictions by Stokes flow (dashed line in Figure 3.2b) through a deformable (liquid metal) matrix to consider this migration process in my experiments. The Stokes prediction is obtained by considering porosity of migrating fluid. The volume of the true migrating fluid is estimated as pore space between the metal phase (ϕ_f). I estimate the total migrating fluid volume by first determining a volume ratio of the known initial metal volume to the observed total volume below LB_{max} . The percentage remaining gives the ambient fluid volume. This pore space is likely overestimated because the observed total volume under LB_{max} is somewhat underestimated as very small particles are still migrating in the mixture layer during this regime. Migration times are well characterized by the Stokes prediction for $\psi < 0.2$. But for higher ψ , the observed migration times are longer than the Stokes prediction. This is likely due to longer and more complex paths that the entrained material must travel through the liquid metal matrix to exit the layer. I plan to add theory for Darcy flow for comparison.

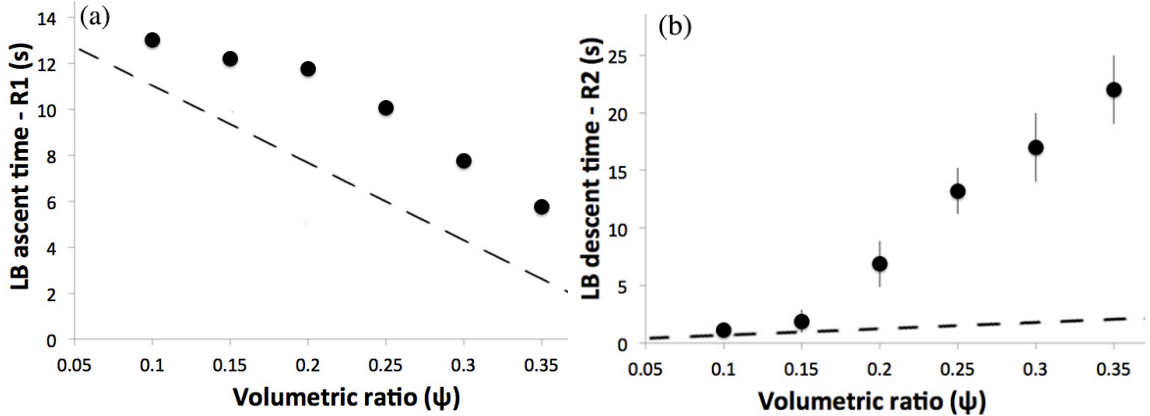


Figure 3.2. (a) The ascent time of the LB in regime 1 is plotted as a function of volumetric ratio, assumed to be caused by metal droplet settling rate. The dashed lines are volumetric Stokes time estimations from (13) and (14). $Re = 0.81$ for $\psi = 0.1$. Re is expected to increase with volumetric ratio in regime 1. (b) The descent time of the LB in regime 2, is assumed to be caused by upward migration of buoyant glucose solution. The Stokes estimation assumes d is the pore diameter filled with ambient fluid, ϕ is porosity of ambient fluid (40 % - 60 %), and μ_m is liquid metal viscosity. Glucose viscosity and density difference are held constant at $\mu = 1.3$ Pa s and $\Delta\rho = 4.58$ g/cm³ respectively. Gallium droplets have an average diameter of $d = 0.27$ cm. Error bars represent one standard error. Points in this figure are obtained from data in Figures 2.4 and 3.1. Therefore, errors from those figures are included the data shown here.

3.1.3 Fluid Entrainment

The lower boundary is observed to rise gradually above the initial boundary during regime 1 and reaches its maximum at the end of this regime in all experiments using liquid metal droplets (see LB_{max} in Figure 3.1). In Figure 3.3a, the maximum height of the lower boundary (LB_{max}) is shown as a function of increasing metal volume. Larger metal fractions clearly result in a higher LB_{max} with a relationship that is roughly linear. I also observed that after separation and compaction is complete and all regimes 1, 2, and 3 are finished (requiring 1-2 days in some cases), the final LB interface is slightly higher than the initial interface (B_i) in all experiments. The difference between the final boundary and B_i is plotted in Figure 3.3b and it is observed that larger volumes of metal

tend to have a greater difference between the two boundaries at the end of the experiment. This suggests that higher volumes of the continuous phase fluid will remain permanently entrained at grain boundaries or in small pockets (although this amount is measured to be small). I have shown in section 2.2 that any influence due to momentum in the starting condition of these experiments will not affect this result. In fact, if present, it would only suggest that this volume of entrainment is a lower bound where slower velocities would have reduced shear resistance and even more entrainment.

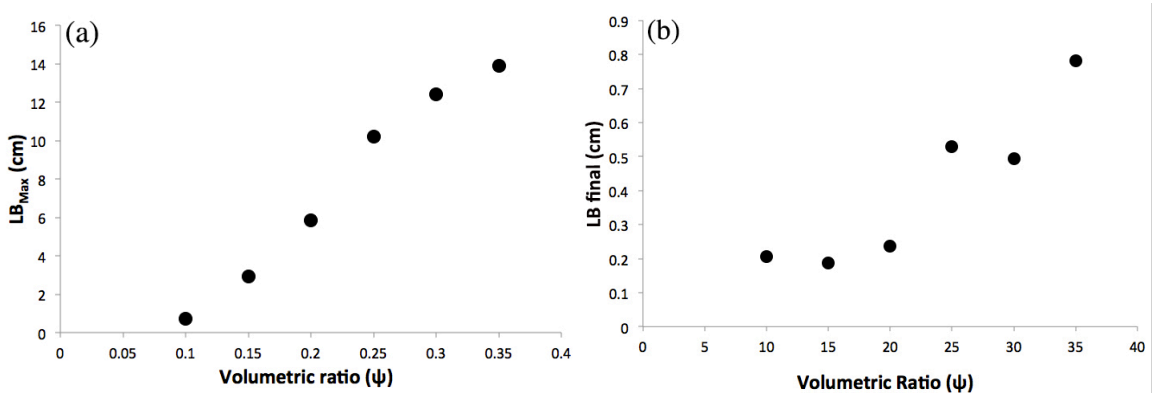


Figure 3.3. Maximum height of the lower boundary (defined from the initial boundary, B_i) as a function of volumetric ratio of liquid metal (ψ) for six experiments (a). The maximum height of the LB increases with increasing liquid metal ratios. Here, glucose viscosity and density difference are held constant at $\mu = 1.3 \text{ Pa s}$ and $\Delta\rho = 4.58 \text{ g/cm}^3$ respectively. Gallium droplets have an average diameter of $d = 0.27 \text{ cm}$ and $Re = 0.81$. Fluid entrainment post compaction (R3) phase is plotted in (b). The final height of the LB after regime 1, 2, and 3 are completed (sometimes after 1-2 days). The final position of the lower boundary (LB final) is measured from the initial B_i interface. This signifies entrainment in the metal core phase that may or may not every migrate out of the matrix.

3.2 Density Difference

3.2.1 Droplet Velocities and Trajectories

In this section, I perform a series of experiments with variable glucose solution densities ranging from $1.312 \text{ g/cm}^3 - 1.605 \text{ g/cm}^3$ corresponding to a density difference

($\Delta\rho = \rho_m - \rho_f$) of $4.305 \text{ g/cm}^3 - 4.598 \text{ g/cm}^3$. I use sodium bromide solutions to obtain density differences without varying fluid viscosity. Experiments show that as $\Delta\rho$ increases (i.e. the continuous phase density decreases), the droplet velocities increase linearly. This is consistent with Stokes law (4) or Darcy law (5) theory only for the experiment with the smallest $\Delta\rho$. However, experimental droplet velocities increase at a rate faster than predicted by either Stokes or Darcy flow. Velocities (within error) may be consistent with Darcy's law (5) for experiments with $\Delta\rho$ above 4.5 g/cm^3 . Experiments with lower $\Delta\rho$ have velocities which are slower than Darcy flow. I demonstrate below that this may be due to particle-particle interactions which act to divert droplets from a vertical descent path.

I attempt to understand this behavior by tracking particles as they descend. The velocities and trajectories of single droplets are tracked using ImageJ and are shown in Figure 3.4b. The droplet exemplified in Figure 3.4a has a diameter $d = 0.45 \text{ cm}$. In Figure 3.4b, trajectories of droplets are shown. Here, droplet diameters vary from $d = 0.14 \text{ cm}$ to $d = 0.32 \text{ cm}$ and are chosen from two separate experiments where $\Delta\rho = 4.305 \text{ g/cm}^3$ (filled symbols) and $\Delta\rho = 4.598 \text{ g/cm}^3$ (open symbols). Trajectories of particles in the experiment with a larger $\Delta\rho$ (open symbols) appear to travel along a more vertical path compared to particles in the experiment with lower $\Delta\rho$ (closed symbols), where more lateral droplet motion displays increased Brownian behavior. I suggest that the change in particle velocities may be due to differences in particle trajectories as they descend. Experiments with low $\Delta\rho$ display more Brownian motion and produce an apparent slower velocity overall. I test this theory by measuring the actual travel distance rather than assuming vertical trajectories of particles traveling down through the fluid column

(Figure 3.4b). This gives an actual velocity which accounts for the particle trajectory path and is shown using a dotted line in Figure 3.4b. This produces a slope that is steeper than Darcy flow and is more consistent with my observed data suggesting Brownian motion is indeed important. Where trajectories are more vertical (high $\Delta\rho$), the dotted line fits data perfectly, however, where trajectories are more chaotic (low $\Delta\rho$), the dotted line is still slightly higher than data. This indicates an underestimation of particle-particle interaction in my tests, which use averages of only a few particles for this estimation.

These particle-particle interaction effects are not considered in Darcy or Stokes flow theory as demonstrated by the poor fit to the data.

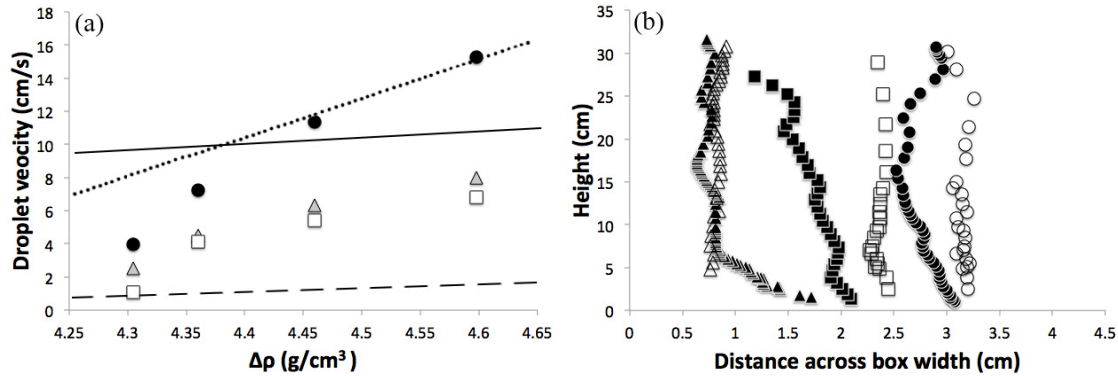


Figure 3.4. Droplets velocities are plotted as a function of density difference $\Delta\rho$ (a) for particles observed in the top 1/3 section of the box (grey triangles), in the 1/3 middle section of the box (closed circles), and in the 1/3 bottom section of the box (Open squares). The droplet diameter is $d = 0.45$ cm, $\psi = 0.1$, $\mu = 0.1$ Pa s, and Re ranges from 0.13 – 0.64. The lowest $\Delta\rho = 4.304$ g/cm³ is considered for (a). Note that points to the left of the graph are on the lower Re range and points to the right of the graph are on the higher Re range. The solid line is estimated from Darcy's law (5) for a single droplet and the dashed line is estimated from Stokes law (4) for a single droplet. The dotted line is calculated using actual distances traveled by particles from Figure (b) rather than the assumption of purely vertical trajectory used to plot closed circles. Figure (b) shows droplet trajectories for two experiments: $\Delta\rho = 4.598$ g/cm³ (closed symbols) and $\Delta\rho = 4.304$ g/cm³ (open symbols). Three particles with different diameters are shown for each experiment. Triangles are droplets with a mean diameter of $d = 0.14$ cm \pm 0.2 cm, squares are droplets with a mean diameter of $d = 0.23$ cm \pm 0.4 cm and circles are droplets with a mean diameter of $d = 0.32$ cm \pm 0.2 cm. The average velocities for closed symbols and open symbols in the middle 1/3 section of the box are 3.99 cm/s and 15.29 cm/s

respectively. The x-axis reflects the actual width of the box and the y-axis is scaled down to exaggerate horizontal droplet movement.

3.2.2 The Lower Boundary Ascent Velocity

I consider growth of the lower boundary from analysis of the boundary heights. The lower boundary ascent velocity is measured and studied as a function of increasing density difference. It is observed that the velocity of the **LB** is approximately constant during regime 1 (e.g. Figure 3.1). A least-squares, best-fit line is obtained for regime 1 and the slope is taken as the **LB** velocity for each experiment. Figure 3.5 shows the result with respect to density difference.

The lower boundary rises at an increasing rate as density difference increases (i.e. as density of the continuous phase fluid decreases). Theoretical approximations for Darcy and Stokes flow are shown for comparison. Here, Stokes flow is estimated using (4) and Darcy flow low is estimated from (15). My experimental results show that Darcy flow over predicts the boundary ascent velocity. Stokes velocity demonstrates a slope and absolute velocity that is most consistent with my data. This may be due the allowance for deformation and viscous drag in the continuous phase in Stokes flow compared to the assumption of a rigid, non-deformable matrix in Darcy flow. This suggests that the increase in $\Delta\rho$ can predominantly explain the increase in **LB** velocity that is observed. The slightly slower velocities in my data may be due to effects from Brownian motion and particle-particle interaction not accounted for in Stokes theory.

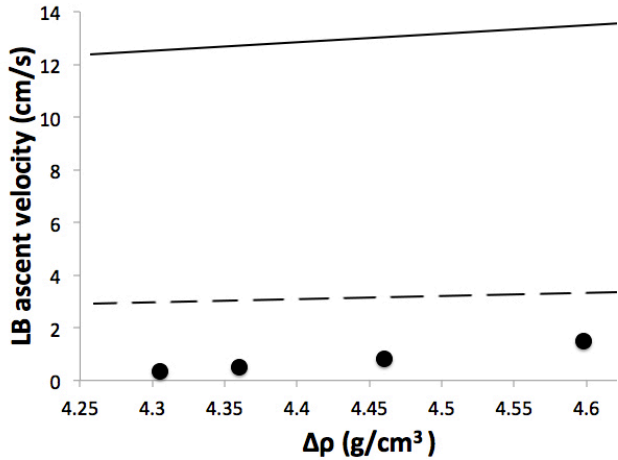


Figure 3.5. Ascent velocity of the lower boundary plotted as a function of density difference $\Delta\rho$. Circles indicate experimentally observed LB velocities. Ascent velocity is calculated from the slope shown in regime 1 as in Figure 3.1. Here, $d = 0.27 \text{ cm} \pm 0.2 \text{ cm}$, $\psi = 0.1$, $\mu = 0.1 \text{ Pa s}$, and Re ranges from $0.13 - 0.64$. The solid line is a volumetric Darcy flow velocity estimated from (15) and the dashed line is a volumetric Stokes flow velocity estimated from (4).

3.3 Metal Droplet Size

3.3.1 Edge Effects and Clustering

Experiments which vary particles size are conducted using rigid, stainless steel precision particles ranging in diameter from $0.16 \text{ cm} - 0.95 \text{ cm}$ with corresponding Bond numbers ranging from $0.06 - 2.1$. I use solid spheres in these experiments to ensure a uniform particle size in each experiment and to maintain a constant viscosity. These experiments show interesting behavior: rigid spheres with larger diameters settle predominantly through the center of the fluid column while particles with smaller diameters tend to migrate and cluster toward fluid column edges (Figure 3.6). This settling that occurs along fluid box walls is most pronounced in Figure 3.6a and 3.6b where Bond numbers are 0.06 and 0.23 respectively. These ‘edge effects’ in my experiments were also present in experiments by Fleck (2011) who observed that when particle size was sufficiently small (i.e. threshold Bond numbers less than 0.05 or metal

droplet diameters below 0.15 cm), gallium droplets adhered to conduit walls. I observe this behavior for experiments with Bond numbers below 0.23 (Figure 3.6 for $d = 0.16$ and 0.32 cm). The slightly higher values observed in my experiments may be due to several factors including the use of a plexiglass wall which may have different adhering properties compared to a plume conduit (Fleck, 2011) that forms within a high viscosity fluid. The difference in physical properties between liquid and solid droplets may also account for this discrepancy.

Particles with the smallest diameters tend to hug the left wall because of the agitation method and a small degree of rotation of the fluid box in the starting conditions of the experiment. But given previous tests (e.g. Fleck, 2011), I am confident this effect would be symmetric along both walls if the agitation method did not involve rotation.

I also observe that rigid particles tend to fall in clusters rather than as single drops compared to liquid droplets. This should cause drops to fall at faster velocities due to an increase in bulk mass for each cluster. Ultimately, this may predict faster metal pond and core formation times. Faster settling velocities also have implications for increased shear heating and supheat in the core (King and Olson, 2011). This is observed for all particle sizes. Further studies should measure the degree of clustering as a function of particle size and falling velocities for clusters in order to compare them to predictions for single drop velocities in a deformable matrix.

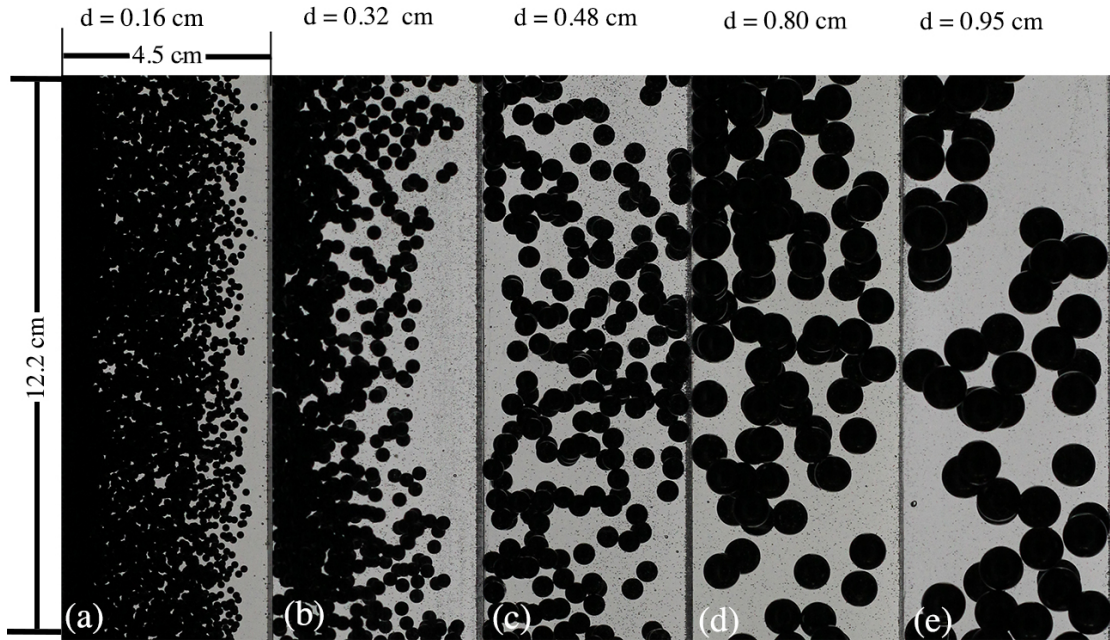


Figure 3.6. Experiments which vary particles size. Here we use solid stainless steel precision spheres. The numbers above indicate particle diameters and for these experiments, $\psi = 0.1$, $\mu = 0.9 \text{ Pa s}$, and $\Delta\rho = 6.650 \text{ g/cm}^3$ are held constant. The Bond numbers vary from 0.06 to 2.1. Note that rigid spheres with larger diameters above 0.32 cm ($Bo = 0.23$) settle predominantly through the center of the fluid column whereas particles with smaller diameters tend to migrate toward fluid column edges.

3.4 Viscosity of Ambient Fluid

In this section, I present results from variable viscosity ratio experiments using rigid stainless steel particles of diameter 0.48 cm with a $\psi = 0.1$ and glucose fluid viscosities ranging from 0.01 Pa s – 80.0 Pa s. I use rigid spheres for these experiments to isolate the effects of fluid viscosity only (see Section 2 on experimental methods). I observe that as viscosity of the ambient fluid increases, the lower boundary ascent velocity decreases (Figure 3.7). I show the growth of the **LB** height with time for each experiment in Figure 3.7a. Notice that the slopes become steeper for decreasing fluid viscosities. The log of the **LB** velocity shown in Figure 3.7b with respect to the log of viscosity demonstrates an exponential relationship. This general behavior can be

estimated by Stokes velocity for solid spheres (where $C = 2/9$) and is given by rearranging (1) as

$$V_{st_solid} = \frac{24\rho g a^2}{9\mu r} \quad (9)$$

which is inversely proportional to viscosity. Equation 9 is plotted in Figure 3.7b (dashed line). Theoretical data plot closest to experimental data for viscosities of 1 Pa s and higher. Experiments with lower glucose viscosities show a more significant deviation from theory. At 0.13 Pa s and 0.03 Pa s, the deviation from theory is 160 % and 180 % respectively. This larger deviation at lower viscosities (governed by Darcy Flow) may occur because Darcy flow applies to flow where inertial forces dominate over viscous forces. At higher viscosities, less particle interaction occurs because higher viscous forces resist or act to dampen chaotic particle behavior. Conversely, at lower viscosities, where inertial forces dominate, contact between particles is important and cause detours from vertical trajectories. This interaction is not accounted for in Stokes law and works to slow experimental velocities compared to theory at the lowest viscosities. This effect will be even stronger if shape changes in particles occur (see next section).

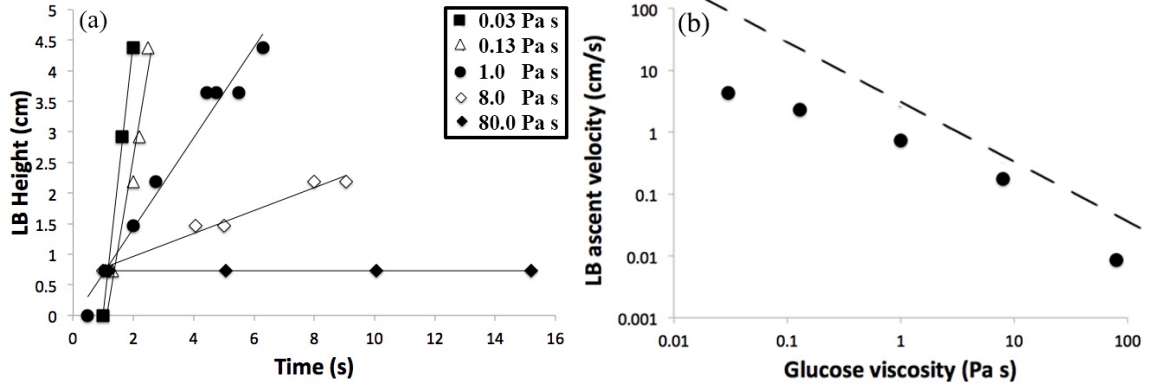


Figure 3.7. Heights of the lower boundaries for variable viscosity ratios are plotted with respect to time. In both (a) and (b), $\psi = 0.1$, $d = 0.48$ cm, and $\Delta\rho = 6.650$ g/cm³ are held constant. (a) For closed squares, $\mu = 0.03$ Pa s, for open triangles, $\mu = 0.13$ Pa s, for closed circles, $\mu = 1.0$ Pa s, for open diamonds, $\mu = 8.0$ Pa s, and for closed diamonds $\mu = 80.0$ Pa s. (b) Log of the **LB** ascent velocity is plotted as a function of Log μ . The dashed line is a Stokes flow estimation from (4).

3.4.1 Shear Force Dependence on Droplet Size

In order to test droplet size dependence on shear force for the case of gallium and glucose solutions, I run a series of three experiments that vary ambient fluid viscosity and use liquid gallium (rather than rigid spheres). Unfortunately, in these experiments both the fluid viscosity and liquid metal drop diameters vary simultaneously as one parameter is dependent on the other using mixing methods in my study. Experimental methods are not altered otherwise. I observe that as viscosity increases, droplet size becomes larger due to reduced shear stresses during agitation (Figure 3.8). This reduction in shear stress is due to slower velocities when higher viscosities are used and applied stress (or agitation) remains constant. I also notice that lower viscosities produce a change in the spherical shape of droplets forming more flattened, ellipsoidal shapes as they descend. These elongated shapes exhibit anisotropic alignment with respect to flow direction. The viscosity ratio λ (6) between the continuous phase fluid and the liquid metal is highest in Figure 3.8a and lowest in Figure 3.8c. I will measure particle velocities to show that

velocities should be faster with the lowest viscosity ratios. This trend is also expected due to the increased diameter of the droplet size itself.

Increasing the ambient fluid viscosity also creates an increase in the volume of observed gallium debris (or residual flakes). This also occurs when larger volumetric ratios are used since more agitation is required to produce a uniform emulsion (and therefore more shear stress is applied). Upon completion of experiments (post regime 3), there is a distinct, measureable layer of gallium debris at the final **LB** (glucose-gallium) interface. I measure and plot the thickness of this layer as a function of volumetric ratio in Figure 3.9. It is observed that as the volume of metal increases, more debris forms. The sub-horizontal surface is due to preferential descending locations on the left side of the tank due to agitation methods (see Section 2). However the fact that this incline is maintained over long times indicates that metal droplets below the **LB** are not fully coalesced and maintain entrained continuous fluid phase material at grain boundaries. Upward migration of the entrained fluids will thus occur over time and subsequently mix with the sediment layer when released. This may be visualized in Figure 3.9b along the fluid wall where droplet shapes are maintained surrounded by continuous phase fluid (although this view of the edge may over estimate the lack of coalescence due to edge effects at the wall).

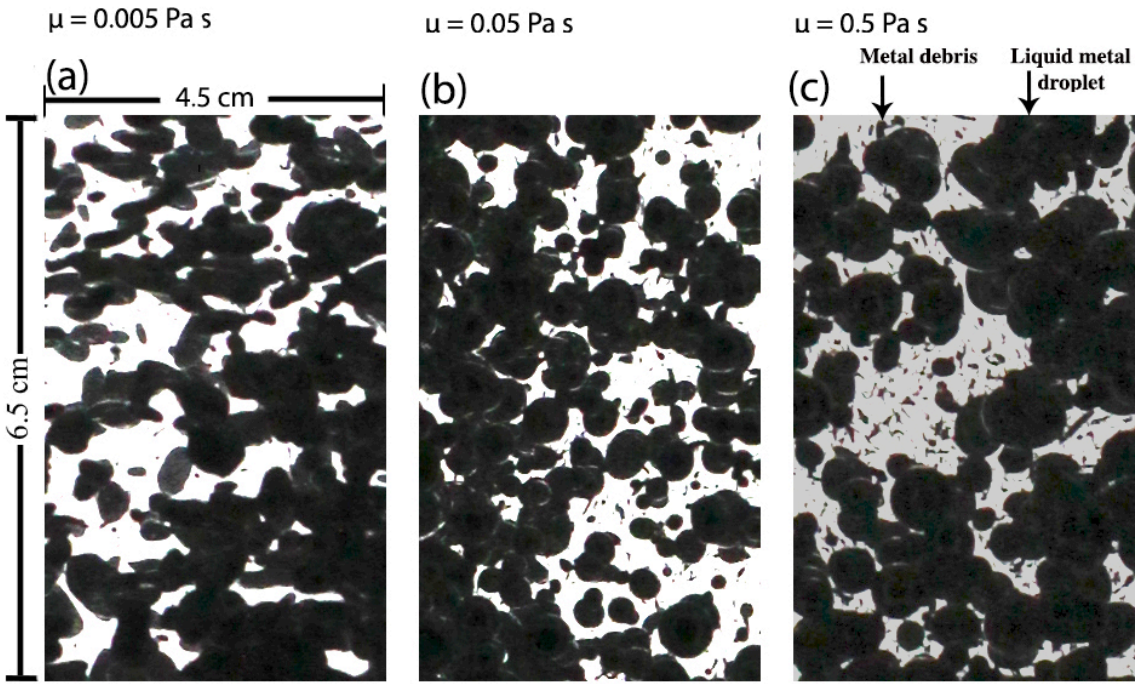


Figure 3.8. Droplet size and shape changes are shown with increasing glucose solution viscosity. For the experiment in (a), $d = 0.22 \text{ cm} \pm 0.14 \text{ cm}$, $\mu = 0.005 \text{ Pa s}$, $\Delta\rho = 4.79 \text{ g/cm}^3$, $\lambda = 2.5$, and $\psi = 0.1$. For (b) $d = 0.33 \text{ cm} \pm 0.2 \text{ cm}$, $\mu = 0.05 \text{ Pa s}$, $\Delta\rho = 4.68 \text{ g/cm}^3$, $\lambda = 25$, and $\psi = 0.1$. For (c), $d = 0.47 \text{ cm} \pm 0.31 \text{ cm}$, $\mu = 0.5 \text{ Pa s}$, $\Delta\rho = 4.62 \text{ g/cm}^3$, $\lambda = 250$, and $\psi = 0.1$. The box dimensions shown are 4.5 cm x 6.5 cm.

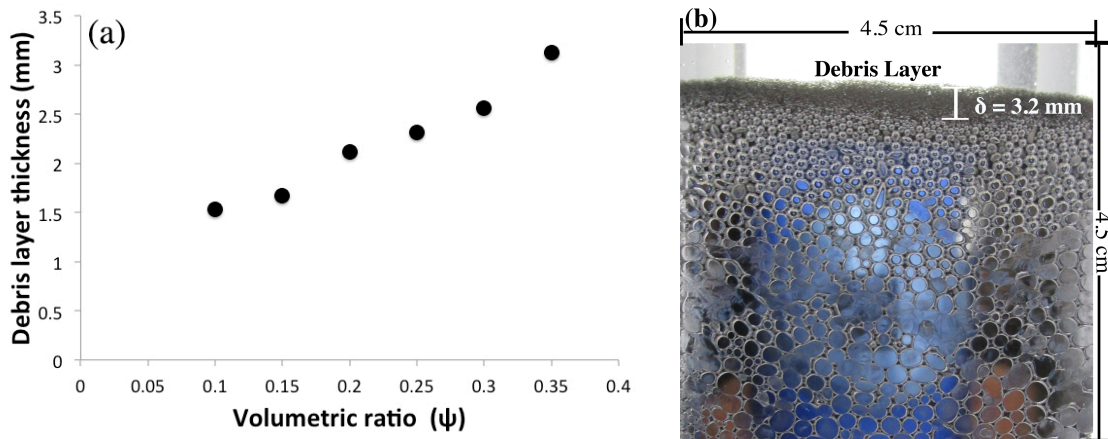


Figure 3.9. Thickness of a residual gallium debris layer (post regime 3) is plotted as a function of volumetric ratio (a) and a visual of the debris layer is shown in (b). This is an experiment having $\mu = 1.3 \text{ Pa s}$, $\psi = 0.35$, $\Delta\rho = 4.58 \text{ g/cm}^3$, and an average diameter $d = 0.27 \text{ cm}$. δ is the sediment layer thickness and is 3.2 mm in its maximum location.

3.5 Liquid Versus Rigid Metal Droplets

I take advantage of my experiments which use both liquid and solid metal spheres to compare the fluid behavior during settling in each case. Comparison of two experiments with solid metal spheres and liquid metal droplets are shown in Figure 3.10. Here I hold constant fluid viscosity, glucose density and volumetric ratio. The droplet diameter is slightly larger for solid spheres (0.42 cm) than for liquid droplets (average 0.27 cm). Thus all physical fluid properties are constant except the metal phase, droplet diameter, and $\Delta\rho$, where stainless steel has a density of $\rho = 7.991 \text{ g/cm}^3$ and liquid gallium has a density of $\rho = 5.991 \text{ g/cm}^3$. This gives $\Delta\rho = 7.291 \text{ g/cm}^3$ for solid spheres and $\Delta\rho = 4.691 \text{ g/cm}^3$ for liquid spheres. Unlike experiments using gallium droplets (filled squares), experiments with steel particles (open circles) demonstrate that the lower boundary never exceeds the initial boundary. This suggests that solid metal spheres do not entrain as much continuous phase fluid as is observed with liquid metal droplets. The degree of entrainment will be controlled by several factors including the speed of the sphere and the nature of flow.

The theoretical \mathbf{LB} ascent slope (and therefore velocity) is plotted for volumetric flow rate in both the case of Darcy flow (15) and Stokes flow (4). Darcy flow velocity is denoted by a solid line and Stokes velocity is dashed. Note that theory plotted here is strictly for liquid metal. Results show that experimental data is lower than Darcy flow and Stokes flow ($C = 1/3$) predictions. But the initial slope for change in boundary height with time for solid spheres is closest to the Darcy prediction and the slower boundary growth is likely caused by the presence of particle-particle interaction during droplet descent as described above. Liquid droplets are visually confirmed to undergo some

degree of shape change as they deform when they approach one another.

Dimpling/flattening of liquid droplets works to slow settling rates and may contribute to the gentler ascent slope compared to theory. It is also observed that the **LB** ascends more slowly in experiments with liquid gallium particles compared to rigid particles. Stokes velocity predicts that rigid spheres ($C = 2/9$) settle slower than deformable droplets ($C = 1/3$) due to increased drag forces. However, the buoyancy ratio is nearly twice as large for experiments with solid particles (slightly higher radius and material density) compared to liquid particles such that this factor overcomes the offset by drag forces. Larger diameters of solid spheres will also contribute to a steeper slope. The slower speed of liquid metal spheres will contribute to increased entrainment of the continuous phase fluid during descent.

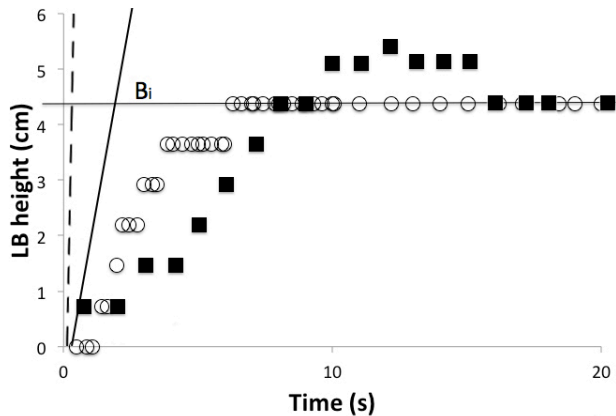


Figure 3.10. A comparison of the **LB** ascent for experiments using rigid metal spheres (open circles) and liquid metal droplets (closed squares). The solid line is the ascent velocity of the **LB** estimated from Darcy's law (15) for liquid gallium and the dashed line is estimated from Stokes law (4) for liquid gallium. The **LB** for liquid metal droplet experiments exceeds the initial boundary (B_i) while rigid spheres do not. For these experiments, $\psi = 0.1$, $d = 0.42$ cm (rigid), $d = 0.27 \text{ cm} \pm 0.18$ cm (average liquid) and $\mu = 1.3 \text{ Pa s}$. $\Delta\rho = 6.650 \text{ g/cm}^3$ for rigid spheres and $\Delta\rho = 4.58 \text{ g/cm}^3$ for liquid droplets. $Re = 1.2$ for rigid spheres and $Re = 0.81$ for liquid droplets.

Chapter 4. Discussion and Geophysical Implications

4.1 Time of Metal Pond and Core Formation

I consider the implications of my experiments for core growth time and the mode of core formation. The time scale of core evolution depends primarily on settling rates of metal. My experiments show a decreased metal settling time with increasing volumetric fractions of metal emulsions (Figure 3.2a) during regime 1. This suggests a shorter core formation time for larger fractions of liquid iron emulsions that form in magma oceans and/or conduits. I find that Stokes flow theory provides the best fit to the laboratory data but is still 32 % faster than observed. This discrepancy is due to the fact that Stokes flow does not account for particle-particle interaction. Since buoyancy ratios and Reynolds numbers used are comparable to those in the Earth, timescales for the Earth's magma oceans and core settling rates can be extrapolated.

Reynolds numbers in my experiments and in the Earth suggest that both Stokes flow and Darcy flow occur in laboratory models as well as in the Earth's magma oceans. Therefore, I model experiments using theory for both regimes with the exception of volumetric ratio experiments. This is due to variable porosity and permeability as the volume of metal is increased which presents difficulties in estimating intrinsic permeability. Future work should better constrain permeability values as a function of volumetric ratio.

Volumetric flow rates governed by Darcy flow are modeled using permeable flow. For simplicity, I assume metal droplets move relative to the stationary ambient fluid during regime 1 and that ambient fluid migrates upward relative to a stationary metal

droplet matrix in regime 2. Darcy's law relates volumetric permeable flow velocity per unit area (\mathbf{Q}_d) to the hydraulic gradient and is given by

$$\mathbf{Q}_d = \frac{\mathbf{K}_\phi \mathbf{Y} \mathbf{A}}{\mu_f} \frac{dh}{dl} \quad (10)$$

where \mathbf{K}_ϕ is permeability and is a measure of droplet shape factor coupled with mean pore diameter, μ_f is the viscosity of the continuous phase fluid, \mathbf{Y} is specific weight, \mathbf{A} is the horizontal cross sectional area, and dh/dl is the hydraulic gradient. In my experiments, hydraulic gradient is assumed to be $dh/dl = 1$ since pressure and droplet velocity are approximately constant in the fluid column. Equation (10) can be expressed in terms of a volumetric Darcy flow velocity as

$$V_d = \frac{K_\phi}{\mu_f} (1-\phi) \Delta \rho g. \quad (11)$$

Note that the full derivation of equation (11) can be referenced in Sato & Sumita (2007). Ranges of values used to calculate V_{st} (which then give theoretical times plotted in Figure 3.2) are summarized in Table 3.

	$\Delta \rho$	ϕ	μ
V_{st} (regime 1)	4.58 g/cm ³	0.1 – 0.35	1.3 Pa s
V_{st} (regime 2)	4.58 g/cm ³	0.37 – 0.56	2.0 x 10 ⁻³ Pa s

Table 3. Summary of values used to estimate Stokes flow velocity V_{st} for volumetric

ratio experiments. Theoretical times for regime 1 and regime 2 are extrapolated using these velocities and are plotted in Figure 3.2.

Porosity is estimated visually from photographs in regime 1 and may be underestimated as integration through the box is not accounted for. In regime 2, porosity is estimated as $1 - (\psi_m / \psi_{total})$. Here, ψ_{total} is the total volume below the maximum height of the lower boundary. This value is overestimated since it assumes that the entire volume of metal is below LB_{max} , however, a small amount of metal still lingers in the upper glucose layer. Since the LB ascent velocity in regime 1 and LB descent velocity in regime 2 are approximately linear, I assume porosity to be constant if the volumetric ratio is constant and confirm this visually in photographs. In order to find K_ϕ , I fit data using equations (10) and (12). Volumetric Darcy flow per unit area Q_d is calculated from

$$Q_d = V_m A \phi \quad (12)$$

where V_m is the velocity of a single metal droplet calculated from (5) and A is pore space area measured from photographs. $V_m = 4.42 \text{ cm/s}$ and A ranges from $10 \text{ cm}^2 - 69 \text{ cm}^2$. Since K_ϕ is the only unknown variable introduced in (10) and (12), I equate the two and plot for variable volumetric fractions. Q_d (12) is plotted with respect to YgA/μ (the known components from (10)) and a linear least-squares method is used to fit the data. K_ϕ is taken as the slope of this line ($7.0 \times 10^{-5} \text{ cm}^2$) and is used to calculate V_d in (11). The theoretical time it takes for metal droplets to settle through the mixture layer (regime 1) and for upward migration of entrained glucose solution (regime 2) is extrapolated using a simple rate equation solved for time

$$t = \frac{36.5 \text{ cm} - LB_{\max}}{2V_{st}} \quad \text{for Stokes flow in regime 1} \quad (13)$$

$$t = \frac{LB_{\max}}{2V_{st}} \quad \text{for Stokes flow in regime 2} \quad (14)$$

and is plotted in Figure 3.2. Here, V_{st} is calculated from (4) and LB_{\max} ranges from 5.11 cm – 28.47 cm. 36.5 cm is the total height of the fluid column and distances are divided by 2 to give the average time using mean settling/migration distances. For regime 1 (Figure 3.2a), settling time decreases with increasing volumetric ratio in both theoretical data and experimental data. However, experimental results require more time for droplets to settle during this regime. In regime 2, the time required for upward migration of low-density fluid is increasing with increasing volumetric ratio and experimental data again plots above Stokes flow estimates (dashed line) in Figure 3.2. This shows that metal ponds and also the lower boundary (analogous to the CMB in the Earth) will grow or rises slower than predicted by Stokes velocities by 32 %. The reduction in settling times may be caused by increased particle-particle interaction in a liquid metal emulsion with multiple droplets. Previous studies have shown that particle interaction increases settling time because the flattening of droplet interfaces, as they approach one another, slows fluid drainage and inhibits subsequent droplet coalescence (Chesters, 1991). Although viscosity ratios used in my experiments are small (resulting in mobile drainage of the continuous phase fluid when droplets are not in contact), gallium droplets experience some deformation when in close proximity and any change from a spherical shape will

reduce settling velocities. Particle interaction which alters a drop from a vertical trajectory will also increase its path length and total descent time.

For experiments in density variations, I closely consider how $\Delta\rho$ affects droplet settling times (Figure 3.4) in regime 1. In (Figure 2.4a), I plot Stokes law (4) and Darcy's law (5) estimates for a single settling droplet. However, experimental droplet velocities are larger than theory predicts for $\Delta\rho \geq 4.35$. The large density difference between liquid metal and dilute glucose solution may be attributed to such behavior. Measurements of particle trajectories (Figure 3.4b) indicate that particle interaction is proportional to their relative densities and in the case of large density contrasts, the droplets do not interact significantly and fall with more vertical trajectories. Decreased fluid interaction and simultaneous droplet deformation suggests rapid and efficient settling of the dispersed metal phase (Loewenberg & Hinch, 1996). These interaction effects are not considered in Darcy or Stokes flow theory. Therefore, higher values of $\Delta\rho$ will result in decreased silicate-iron droplet interaction and hence, faster core formation times.

In order to compare settling velocities of single droplets to volumetric flow rates, the lower boundary ascent velocity is modeled in Figure 3.5. I use Darcy's law (11) modified to model the **LB** behavior (solid line)

$$V_{d_LB} = \frac{K_\phi}{\mu_f} (1-\phi_{LB}) \Delta \rho g \quad (15)$$

where $\mu_f = 0.7 \text{ Pa s}$, ϕ_{LB} is the porosity near the lower boundary (above the lower boundary) and ranges from 0.41 – 0.46, and $\Delta\rho$ ranges from 4.305 g/cm^3 – 4.598 g/cm^3 . K_ϕ and ϕ_{LB} are identified using the same method described previously in this section with

attention focused on the area directly above the ***LB***. The volumetric Stokes flow (4) model is also plotted (dashed line) in Figure 3.5. The constant, slower velocities that occur below $\Delta\rho = 4.4 \text{ g/cm}^3$ may be due to increased particle interaction and deflection not accounted for in static permeability estimates. Above $\Delta\rho = 4.4 \text{ g/cm}^3$, (as is the case for single particle velocities) ***LB*** ascent velocities are faster and approach the Stokes prediction because it is likely that less particle interaction occurs when buoyancy ratios between metal and the ambient fluid are larger.

The shallow slope in theoretical lines plotted for all density difference experiments suggests that density variations of the continuous phase glucose fluid only place small constraints on boundary and droplet velocities. However, experimental results show that the boundary ascent velocity has a steeper slope than theory predicts, which is evidence that density changes may play an important role in ***LB*** ascent velocity and core formation time.

A lower density of magma ocean material has implications for more rapid core growth due to faster settling of metal droplets and vice versa (Figures 3.4 and 3.5). A larger density difference between core forming metal and silicate melt may further contribute to accelerated core formation time since metal can more efficiently segregate from a magma ocean and/or conduit. Larger densities of ambient fluid (lower $\Delta\rho$) tested experimentally suggest slower formation time of a metal pond compared to Stokes flow and therefore, slower formation of the Earth's core. This is important because previous studies show that the range of $\Delta\rho$ in a magma ocean can extend from 4.05 g/cm^3 to 4.55 g/cm^3 due to density variations of silicate melts (Fu and Elkins-Tanton, 2014). Chemical compositions on chondritic meteorites can vary significantly and fractional crystallization

of silicate material post impact can greatly affect the magma ocean density (Fu and Elkins-Tanton, 2014). I explore most of the range of $\Delta\rho$ suggested here except for the lowest values around 4.05 g/cm³. The difference between Stokes theory and my results are within 158 % (Figure 3.5). Therefore, ***LB*** rise velocities are not precisely predicted by Stokes equation (4) for most of my experiment, but specifically for low density magmas. At lower values $\Delta\rho$ (around 4.05 g/cm³) shown by Fu and Elkins-Tanton (2014), this discrepancy in prediction is expected to increase based on data plotted in Figure 3.5.

My experiments show that high $\Delta\rho$ produces higher droplet velocities (Figure 3.4a). Higher $\Delta\rho$ values in a magma ocean will also have implications for increased shear heating due to higher droplet settling velocities. This can contribute to the core superheat observed today as estimated in previous studies using computer numerical solutions (King and Olson, 2011).

4.2 Entrainment and Light Elements in the Core

Entrainment of low-density glucose provides a model for light element transport to the core. My results show that metal ponds consisting of liquid metal emulsions have important implications for entrainment of magma into a metal pond and into the core itself. Larger volumes of metal emulsions increases droplet surface area availability for glucose coating and therefore, increased downward entrainment of glucose solution. Previous studies of particles descending through a stratified fluid implied that three droplets descending together entrained more than triple the amount of material entrained by a single droplet (Manga and Stone, 1995). Future work will measure and confirm the magnitude of entrainment for multiple drops to provide a framework for comparison with

results shown here. The time scale for regime 2 (Figure 3.2b) indicates the rate of upward migration of entrained fluid is slowed. This, coupled with larger amounts of fluid entrainment is a principal mechanism for core-mantle equilibration.

The final location of the **LB** after long times (1-2 days) is found to occur above the initial fluid boundary and indicates that low-density glucose material is permanently entrained below the **LB** within the liquid metal layer, likely at grain boundaries and in small (~ 0.1 mm) pockets visible at box edges. This can be interpreted to happen because gallium droplets have a large interfacial surface tension in dilute glucose and therefore resist further deformation and coalescence (Sato & Sumita, 2007). This apparent entrainment is shown to increase with increasing volumetric ratios of fluids (Figure 3.3a) and is also expected to increase with lower viscosity ratios (Figure 3.8) due to several factors including changes in shear stress and shape change of descending metal droplets. Figure 3.9b further shows that close packing of metal occurs during regime 3 and exhibits a dominant hexagonal structure that is achieved because droplets are deformable and smaller droplets tend to fill interstitial spaces between larger droplets. The slow compaction (accounting for $> 99.9\%$ of the experiment duration time) that occurs during regime 2 and regime 3 provides the opportunity for silicate material to be in contact with core forming metals over a prolonged period of time. Due to high pressures and temperatures in the core, partitioning of light elements in the core is more readily achieved (Rubie et al., 2007). Therefore, material that experiences metal-silicate equilibration in the mantle can happen from the bottom-up as well as from the top-down. This may have further contributions to the widespread siderophile abundance problem discussed below.

Experiments also show that liquid metal droplets will entrain significantly more magma material than solid metal particles. In general, liquid droplets are not subject to shear stresses but are subject to normal stresses and the opposite is true for solid spheres. This is a very important distinction between deformable droplets and rigid particles because it implies that solids should entrain more material than liquids during descent. However, I observe significantly more entrainment in cases with liquid metal. I suggest that rigid spheres behave differently than expected when being compacted. Because solid spheres do not deform when they come in contact with one another, they may drive fluid out between pore spaces more efficiently. This added pressure force is additional to buoyancy forces inherent in the entrained fluid and aids in upward migration of low-density material.

Liquid droplets deform easily when they contact another droplet and this is not efficient in expelling continuous phase fluid. Therefore fluid escapes predominantly through buoyancy forces alone taking longer to exit the liquid metal matrix. This distinction between solid and liquid phase metal implies that solid metal particles in a magma ocean or conduit contribute less silicate melt entrainment in the core and less metal-silicate equilibration as a result.

Previous studies using numerical calculations showed that shear heating is an active process during iron metal descent to the core due to rapid descent velocities of metal in a magma ocean and it is sufficient to maintain a molten state to great depths even to the lower mantle (King and Olson, 2011). If iron metals are able to maintain a molten state during descent through a magma ocean, or through the conduit of a descending metal plume (Nguyen, 2010; Fleck, 2011), then light elements and silicates

will be entrained into the core itself. The residence time of the magma phase in grain boundaries between iron metal drops will be longer with fully liquid phase droplets and may stay for very long periods of time as shown by regime 3 (Figure 3.1). I will use theoretical predictions from Stokes flow as shown in Figure 3.2b to estimate the time required for fluid migration out of the core during early Earth differentiation. I expect predictions for migration times to be underestimated which may be further delayed by high pressures at the CMB not considered in my experiments. This increased residence time also provides a mechanism for iron-silicate equilibration and upward release of siderophile elements into the lower mantle.

I note that other factors such as buoyancy ratio, particle size, or viscosity have a lesser effect. The \mathbf{LB} exceeds the \mathbf{B}_i for variable $\Delta\rho$ experiments, but it is only 2.7% and is roughly constant for all experiments. Thus density difference does not strongly influence the degree of entrainment.

4.3 The Siderophile Abundance Problem

I consider implications regarding the ‘excess siderophile element problem’ in the Earth’s upper mantle (Ringwood, 1977) and suggest three primary explanations for this observation. First, emulsions provide a larger surface area for iron-silicate equilibration and thus more siderophile elements may be left in the mantle during settling processes. In addition, smaller droplets settle at slower velocities compared large bodies of metal, allowing more time for equilibration to occur. The observation that smaller droplets settle more slowly along fluid column walls suggests that in the case of threshold Bond numbers (e.g. Fleck, 2011), liquid iron droplets travel along conduit walls for extended

periods of time. This pathway and reduced travel time will provide additional time for metal-silicate equilibration in conduits. Second, I observe a metal sediment layer that forms above the metallic core after settling. If this sediment layer is stable, it may be entrained in upwelling mantle plumes over the Earth's history and equilibrate with mantle minerals. Finally, the upward migration process of light elements out of the core proceeds over times longer than metal-silicate diffusion times. This will transport additional siderophile elements into the lower mantle. In my experiments, migration is not restricted to conduits but occurs anywhere along the CMB, providing an avenue for siderophile elements to mix with the Earth's mantle.

The time for upward migration of ambient fluid in regime two (Figure 3.2b) is calculated for the case of entrained magma material within a trailing conduit in the Earth using Stokes equation (4) and (14). Two cases are extrapolated: 1) 20% of Earth's current core volume formed from metal emulsions and 2) 50% of Earth's current core volume formed from metal emulsions (see Fleck et al., 2010 for the style of metal emulsion descent in the form of diapirs). An original radius of 3,400 km is assumed. Approximate densities for liquid iron ($\rho_m = 9.0 \text{ g/cm}^3$) and silicate melt near the core ($\rho_f = 3.0 \text{ g/cm}^3 - 5.0 \text{ g/cm}^3$) are used. I use a range of liquid iron viscosities from $3.0 \times 10^{-1} \text{ Pa s} - 3.0 \text{ Pa s}$ since high pressures near the core may produce higher viscosities. For case 1, the porosity (37 %) and pore diameter ($\sim 0.30 \text{ cm}$) are taken from my experimental observations and applied to the Earth. A time correction of 14% is accounted for due to the discrepancy between observed times and Stokes prediction (Figure 3.4b). My calculations show a range of times in case 1 from 3.5 hours – 14.5 days. Because these numbers appear to be quite small with respect to Earth's formation time, I suggest that

the viscosity difference may be very important here and perhaps should be accounted for. If μ is replaced with $\Delta\mu$ in (14), assuming a magma ocean viscosity of 1000 Pa s and an iron viscosity of 0.3 Pa s. I estimate it takes \sim 110 years for upward migration across the CMB that was originally entrained in the Earth's core during its formation. Since case two was not a variable included in my volumetric ratio experiments, I extrapolate porosity to be 72 %, a pore diameter of 0.1 cm is assumed, and a time correction of 28% (from Figure 3.2b) is applied to case 2. Considering $\Delta\mu$ here with the same magma ocean and iron viscosities assumed in case 1, and extrapolated 28% correction (from Figure 3.2b), I show that it takes 1,300 years for upward migration of magma across the CMB. These times are fast but are expected considering the large buoyancy ratios between the metal and magma materials.

The estimated time required for an iron droplet to re-equilibrate with silicate magma can be calculated as $t = r^2/\kappa$, where r is the radius of a droplet and κ is mass diffusivity. Assuming a droplet radius of 1 cm (suggested by Rubie et al., 2007) and $\kappa = 1 \times 10^{-10} \text{ m}^2/\text{s}$, time required for re-equilibration is 2.4 years. If a critical radius (the radius above which a droplet will not chemically equilibrate with a magma ocean (Olson and Weeraratne, 2008)) $r = 25 \text{ cm}$ is considered, a time of 80.0 years is estimated. This suggests that smaller droplets will equilibrate in a shorter period of time. If I compare the diffusion time to the time calculated for magma migration in regime 2, I show that diffusion times across individual emulsion iron droplets are shorter than the total migration times. This is sufficient for chemical re-equilibration of iron and silicate material and will carry siderophile elements within the migrating magma from the core

across the CMB into the lower mantle and may address the siderophile abundance problem.

4.4 Metal Sediment at the Core-Mantle Boundary

The existence of an ultra low velocity zone (ULVZ) at the core-mantle boundary (CMB) has been observed from seismic data (e.g. Grand, 1994; Woodward & Dziewonski, 1994; Romanowicz, 1996). Previous interpretations for this anomaly include pockets of dense partial melt (Williams & Garnero, 1996), remnants of a basal magma ocean (Labrosse et al., 2013), and the accumulation of silicate sediment on the CMB (Buffett et al., 2000). However, theoretical models are still a topic of debate. My physical experiments show that during emulsion droplet descent, a metal debris or residue forms due to shear stresses between the ambient fluid and liquid metal droplets. While the metal droplets fall quickly forming the proto-core, the metal debris settles much slower and later accumulates as a layer of metal sediment above the liquid metal layer (analogous to the region above the CMB), (Figure 3.9b). My experiments support the case for a high-density sediment layer at the CMB. However, I suggest these sediments may be a mixture of silicate and metallic composition. This is also consistent with low viscosities required for the ULVZ layer (Jellinek and Manga, 2002). A conductive layer at the CMB may be explained by anomalous dissipation in Earth's annual nutation and therefore, reinforces the theory of metal sediment accumulation (Buffett, 1992). In this case, iron sediments will expel the majority of silicate material but leave a small amount of light elements behind in the sediment layer. It is unknown whether this metal sediment accumulating at the CMB is later entrained due to vigorous convection of the outer core. Light elements

mixed in the metal debris may be pulled into the core as a result and equilibration will occur. This mechanism can thus explain the core density deficit observed today (Birch, 1952; Anderson and Isaak, 2002).

The entrainment of magma into the core and subsequent slow migration of these light element upward will also enhance convection in the outer core contributing increased power to maintain the geodynamo. The release of light elements from the initial forming metals will leave behind a dense metal phase that will sink to the center of the core, initiating convection contributing power to the geodynamo (Buffett et al., 2000). My results show this upward migration of light elements out of the core is rapid, immediately following core formation events but proceeds slowly in regime 2. This suggests that the geodynamo would be stronger in the early Earth and decrease in strength with time. Note that the upward migration times of low-density fluids are underestimated here where high pressures in the core, which will act to slow migration of light elements, is not considered. The metal sediment layer at the base of the mantle may be entrained in upwelling mantle plumes, providing chemical signatures observed in island arcs and mantle plumes (Buffett et al., 2000)

Chapter 6. Summary

I have conducted a series of experiments on gravitational settling of liquid metal droplets and solid metal spheres through glucose solutions. I vary volumetric ratios, density ratios, viscosity ratios and droplet diameters. Laboratory models as well as magma oceans have Reynolds numbers that integrate Stokes and Darcy theory and

therefore, I use both flow regimes to model my data. I ultimately show that Stokes flow theory is a better fit to experimental data than Darcy flow theory. For all liquid metal experiments, three distinct stages are observed. Regime 1 reveals rapid sinking of metal droplets that are coated with low-density fluid, regime 2 is characterized by a fast upward migration of entrained fluid and regime 3 couples slow compaction of metal droplets at the base with final segregation of residual glucose solution. The lower boundary ascent velocity is governed primarily by viscosity ratios and has implications for metal pond and core formation time. I show that metal droplets settle faster through magma oceans with lower densities than is predicted by theory. This can be interpreted to occur because larger density differences between binary immiscible fluids decreases droplet interaction (which causes deformation) and allows for droplets to more efficiently settle. The volumetric ratio of metal to silicate magmas is shown to have the strongest effect on the degree of entrainment of magma into a metal pond and into the core. Specifically, the lower boundary descent time is longer with higher volumetric fractions of metal, indicating that metal-silicate equilibration time is higher with larger volumes of metal. Experiments with liquid metal versus solid metal phases further indicate that liquids entrain more than solids which is contrary theoretical predictions. This may be explained by particle rigidity. Solid spheres can efficiently drive out continuous phase fluid while liquid droplets deform when they approach one another and thereby trap low-density fluid. The degree and time duration of entrainment is important because it may be evidence for the presence of light elements in the core and for “bottom-up” metal-silicate equilibration. I estimate the time for upward migration of buoyant, silicate material in the Earth to range from 3.5 hours – 1,300 years for several possible core-formation scenarios.

The time for re-equilibration of iron in a magma ocean is also calculated for comparison and ranges from 578 days – 80 years for droplets with radius $r = 1$ cm and $r = 25$ cm respectively. Therefore, in the case of small metal droplets, it is possible for metal-silicate equilibration to occur quickly during upward migration of entrained, low-density silicate material. This suggests that metal emulsions provide a much larger surface area between metals and silicates to allow for chemical equilibration and address the excess siderophile observation while still descending rapidly enough to form a core in 30 Myr.

Chapter 7. Future Work

In this chapter, I list future work that will advance this research, help quantify my results, and increase laboratory method efficiency.

- 1) I recommend future studies measure shape changes for each experiment and compare with theory for droplet velocity in order to ascertain how velocity is affected by differing degrees of deformation.
- 2) Develop Stokes velocity theory for flow through multiple droplets having some degree of porosity. It will likely include a drag coefficient that may differ when droplets interact with various quantities of neighboring droplets. This new theoretical line should be added to Figure 3.2.
- 3) Measure and confirm the magnitude of entrainment for multiple drops to provide a framework for comparison with results shown here.
- 4) Variable viscosity experiments should be conducted with liquid gallium if it is possible to somehow maintain a constant droplet size. Future work may also involve

investigating more in depth the effects of viscosity change on droplet size and shape. I recommend pouring a solid stream of gallium into variable viscosity solutions and measuring size and shape of sheared droplets.

- 5) Measure the velocity of boundaries during R3.
- 6) Use of video camera to capture droplet velocities with more ease.
- 7) Combine with work by fleck to show a larger scale picture. Studies should be conducted in a larger frame of reference which includes conduits settling through a high viscosity fluid.
- 8) Measure further effects of density difference. Does density difference influence the drag coefficient? Although for the Stokes drag coefficient, density difference is neglected, however, this should be tested experimentally. Also further theoretical studies of this may be needed.
- 9) Test if gallium in R3 entrains metal sediment. In order to test this, continue to run an experiment with a layer of metal sediments using a heat source below the fluid column to create convection in the gallium layer.
- 10) Further studies should measure the degree of clustering as a function of particle size and falling velocities for clusters and compare them to predictions for single drop velocities in a deformable matrix. Do this for liquid and solid spheres.
- 11) Measure the debris layer for the viscosity experiments (Figure 3.8). Do a full set of these and measure it. Even though drop size is also changing, this will be interesting.

References

- Anderson, O.L., & Isaak, D.G., 2002, Another look at the core density deficit of Earth's outer core. *Physics of the Earth and Planetary Interiors*, 131, 19-27 P.
- Birch, F., 1952, Elasticity and constitution of the Earth's interior. *Journal of Geophysical Research*, 57, 227-286 P.
- Buffett, B.A., 1992, Constraints on magnetic energy and mantle conductivity from the forced nutations of the Earth. *Journal of Geophysical Research*, 97, 19,581-19,597 P.
- Buffett, B.A., Garnero, E.J., and Jeanloz, R., 2000, Sediments at the top of the Earth's core. *Science* 290, 1338-1342 P.
- Chabot, N.L., Draper, D.S., & Agee, C.B., 2005, Conditions of core formation in the Earth: constraints from nickel and cobalt partitioning. *Geochimica et Cosmochimica Acta* 69, 2141-2151 P.
- Chesters, A.K., 1991, The modeling of coalescence processes in fluid-liquid dispersions: A review of current understanding. *Transactions of the Institution of Chemical Engineers*, 69, 259-270 P.
- Fleck, J., 2011, Tharsis Formation from Density Driven Thermo-Chemical Plumes During Planetary Differentiation [MS thesis]: Northridge, California State University, X p.
- Fu, R.R., Elkins-Tanton, L.T., 2014, The fate of magmas in planetesimals and the retention of primitive chondritic crusts. *Earth and Planetary Science Letters*, 390, 128-137 P.
- Grand, S.P., 1994, Mantle shear structure beneath the Americas and surrounding oceans. *Journal of Geophysical Research*, 99, 11,591-11,621 P.
- Höink, T., Schmalz, J., and Hansen, U., 2006, Dynamics of metal-silicate separation in a terrestrial magma ocean. *Geochemistry Geophysics Geosystems* 7: Q09008 (doi: 10.1029/2006GC001268)
- Helffrich, G., and Kaneshima, S., 2004, Seismological constraints on core composition from Fe-O-S liquid immiscibility. *Science* 306, 2239-2242 P.
- Honda, R., Mizutani, H., & Yamamoto, T. 1993, Numerical simulations of Earth's core formation. *Journal of Geophysical Research*, 98, 2075-2089 P.
- Jacobsen S.B., 2005, The Hf-W isotopic system and the origin of the Earth and Moon. *Annual Review of the Earth and Planetary Sciences* 33, 531-570 P.
- Jellinek A.M., Manga, M., 2002, The influence of a chemical boundary layer on the fixity, spacing and lifetime of mantle plumes. *Letters to Nature*, 418, 760 – 763 P.
- Karato, S.I., and Murthy, V.R, 1997, Core formation and chemical equilibrium in the Earth. Part 1: Physical considerations. *Physics of the Earth and Planetary Interiors*, 100, 61-79 P.
- King, C., Olson, P., 2011, Heat partitioning in metal-silicate plumes during Earth differentiation. *Earth and Planetary Science Letters*, 304, 577-586 P.
- Klein, T., Munker, C., Mezger, K. & Palme, H. 2002, Rapid accretion and early core formation on asteroids and the terrestrial planets from Hf-W chronometry. *Nature* 418, 952 – 955 P.
- Kohlstedt, D.L., Zimmerman, M.E., 1996, Rheology of partially molten mantle rocks. *Annual Review of Earth and Planetary Science*, 24, 41-62 P.
- Labrosse, S., Hernlund, J.W., and Coltice N., A crystallizing dense magma ocean at the base of the Earth's mantle. *Nature*, 450 (7171), 86-869 P.

- Loewenberg, M., & Hinch, E.J., 1996, Numerical simulation of a concentrated emulsion shear flow. *Journal of Fluid Mechanics*, 321, 395-419 P.
- Manga, M., & Stone, H.A., 1995, Low Reynolds number motion of bubbles, drops and rigid spheres through fluid-fluid interfaces. *Journal of Fluid Mechanics*, 287, 279-298 P.
- Minarik, W.G., Ryerson, F.J., Watson, E.B., 1996, Textural entrapment of core-forming melts. *Science*, 272, 530-533 P.
- Nguyen, C., 2010, Study of Trailing Conduits in high Bond Number Metal-Silicate Plumes During Core Formation [MS thesis]: Northridge, California State University, 1-164 p.
- Olson, P., and Weeraratne, D., 2008, Experiments on metal-silicate plumes and core formation. *Philosophical Transactions of the Royal Society, ser. A*, v. 366, 4253-4271 p.
- Pahlevan, K., & Stevenson, D.J., 2007, Equilibration in the aftermath of the lunar-forming giant impact. *Earth Planetary Science Letters*, 262, 438-449 P.
- Rains, C., 2014, Descent of low Bond number liquid-metal plumes with trailing conduits during core formation [MS thesis]: Northridge, California State University, X P.
- Righter, K. & Drake, M.J., 2000, Metal/silicate equilibrium in the early Earth – new constraints from the volatile moderately siderophile elements Ga, Cu, P and Sn. *Geochimica et Cosmochimia Acta* 64, 3581-3597 P.
- Ringwood, A.E., 1966, High-pressure transformations in Pyroxenes. *Earth and Planetary Science Letters*, 1, 351-357 P.
- Ringwood, A.E., 1977, Composition of the core and implications for the origin of the Earth. *Geochemical Journal*, 11, 111-135 P.
- Romanowicz, B., Li, X.D., Durek, J., 1996, Anisotropy in the inner core; could it be due to low-order convection?, *Science*, 274, 963-966 P.
- Rubie, D.C., Melosh, H. J., Reid, J. E., Liebske, C. & Righter, K., 2003, Mechanisms of metal-silicate Equilibration in the terrestrial magma ocean. *Earth Planet. Sci. Lett.* 205, 239-255 p.
- Rubie, D.C., Nimmo, F., & Melosh, H.J., 2007, in Treatise on Geophysics Vol.9 (ed. Schubert, G.) 51-90 (Elsevier, Amsterdam)
- Rushmer T, Minarik WG, and Taylor GJ, 2000, Physical processes of core formation. In: Canup RM and Righter K (eds.) *Origin of the Earth and Moon*, pp 227-244. Tucson, AZ: University of Arizona Press.
- Sato, M., and Sumita, I., 2007, Experiments on gravitational phase separation of binary immiscible fluids: *Journal of Fluid Mechanics*, v. 000, 1-31 p.
- Shannon, M.C., Agee, C.B., 1996, High pressure constraints on percolative core formation. *Geophysical Research Letters*, 20, 2717 – 2720 P.
- Solomatov, V., 2000, Fluid dynamics of a terrestrial magma ocean. In *Origin of the Earth and Moon* (eds R. Canup & K. Righter), pp. 323 – 338. Tucson, AZ: University of Arisona Press.
- Solomatov, V., 2007, in Treatise on Geophysics Vol. 9 (ed. Schubert, G.), 91-119 (Elsevier, Amsterdam)
- Stevenson, D. J., 1990, Fluid Dynamics of Core Formation: *Origin of the Earth* (eds N.E. Newsom & J. H. Jones), New york, NY: Oxford University Press, 231-249 p.

- Tonks W.B., & Melosh, H.J., 1993, Magma ocean formation due to giant impacts. *Journal of Geophysical Research*, 98, 5319-5333 P.
- Wang, H., Zinchenko, A., & Davis, R.H., 1994, The collision rate of small drops in linear flow fields. *Journal of Fluid Mechanics*, 265, 161-188 P.
- Williams, Q., Garnero, E.J., 1996, Seismic evidence for partial melt at the base of Earth's mantle. *Science*, 273, 1528-1530 P.
- Wood, B. J., Walter, M.J. & Wade, J. 2006 Accretion of the Earth and segregation of its Core. *Nature*, v. 441, 825-833 p.
- Woodward, R.L., Dziewonski, A.M., 1994, Comparisons of seismic heterogeneity models and convective flow calculations. *Geophysical Research Letters*, 21, 325-328 P.
- Yiantsios, S.G., & Davis, R.H., 1990, On the buoyancy-driven motion of a drop towards a rigid surface or a deformable interface. *Journal of Fluid Mechanics*, 217, 547-573 P.
- Yin Q.Z., Jacobsen, S.B., Yamashita, K., Blichert-Toft, J., Telouk P., & Albarede F., 2002, A short timescale for terrestrial planet formation from Hf-W chronometry of meteorites. *Nature* 418: 949-952 P.
- Yoon, Y., Borrell, M., Park, C.C., & Leal, L.G., 2005, Viscosity ratio effects on the coalescence of two equal-sized drops in a two-dimensional linear flow. *Journal of Fluid Mechanics*, 525, 355-379 P.
- Yoshino, T., Walter, M.J. and Katsura, T., 2003, Core formation in planitesimals triggered by permeable flow. *Nature*, 422, 154-157 P.